

# The Tully–Fisher relation of COLD GASS Galaxies

Alfred L. Tiley,<sup>1★</sup> Martin Bureau,<sup>1</sup> Amélie Saintonge,<sup>2</sup> Selcuk Topal,<sup>1</sup>  
Timothy A. Davis<sup>3,4</sup> and Kazufumi Torii<sup>5</sup>

<sup>1</sup>Department of Physics, Sub-department of Astrophysics, University of Oxford, Denys Wilkinson Building, Keble Road, Oxford OX1 3RH, UK

<sup>2</sup>Department of Physics and Astronomy, University College London, Gower Place, London WC1E 6BT, UK

<sup>3</sup>Centre for Astrophysics Research, University of Hertfordshire, Hatfield, Herts AL10 9AB, UK

<sup>4</sup>School of Physics and Astronomy, Cardiff University, Queens Buildings, The Parade, Cardiff CF24 3AA, UK

<sup>5</sup>Department of Physics, Nagoya University, Chikusa-ku, Nagoya, Aichi 464-8601, Japan

Accepted 2016 June 22. Received 2016 June 22; in original form 2016 March 25

## ABSTRACT

We present the stellar mass ( $M_*$ ) and *Wide-Field Infrared Survey Explorer* absolute Band 1 magnitude ( $M_{W1}$ ) Tully–Fisher relations (TFRs) of subsets of galaxies from the CO Legacy Database for the *GALEX* Arecibo SDSS Survey (COLD GASS). We examine the benefits and drawbacks of several commonly used fitting functions in the context of measuring CO(1–0) linewidths (and thus rotation velocities), favouring the Gaussian Double Peak function. We find the  $M_{W1}$  and  $M_*$  TFR, for a carefully selected sub-sample, to be  $M_{W1} = (-7.1 \pm 0.6)[\log(\frac{W_{50}/\sin i}{\text{km s}^{-1}}) - 2.58] - 23.83 \pm 0.09$  and  $\log(M_*/M_\odot) = (3.3 \pm 0.3)[\log(\frac{W_{50}/\sin i}{\text{km s}^{-1}}) - 2.58] + 10.51 \pm 0.04$ , respectively, where  $W_{50}$  is the width of a galaxy’s CO(1–0) integrated profile at 50 per cent of its maximum and the inclination  $i$  is derived from the galaxy axial ratio measured on the Sloan Digitized Sky Survey  $r$ -band image. We find no evidence for any significant offset between the TFRs of COLD GASS galaxies and those of comparison samples of similar redshifts and morphologies. The slope of the COLD GASS  $M_*$  TFR agrees with the relation of Pizagno et al. However, we measure a comparatively shallower slope for the COLD GASS  $M_{W1}$  TFR as compared to the relation of Tully & Pierce. We attribute this to the fact that the COLD GASS sample comprises galaxies of various (late-type) morphologies. Nevertheless, our work provides a robust reference point with which to compare future CO TFR studies.

**Key words:** galaxies: general.

## 1 INTRODUCTION

### 1.1 Background

The Tully–Fisher relation (TFR; Tully & Fisher 1977), one of the best studied galaxy scaling relations, can be derived easily by considering circular motion under gravity from a spherical mass distribution:  $M(r) \propto v^2(r)r$ , where  $M$  is the mass of the body enclosed within a radial distance  $r$  from its centre and  $v$  is the rotational velocity at  $r$ . Defining the dynamical mass-to-light ratio  $M/L$  and surface mass density  $\Sigma \equiv M/\pi r^2$  of the body, one then obtains the TFR:

$$L \propto \frac{v^4}{\Sigma(M/L)}. \quad (1)$$

Discovered observationally, the TFR was initially used as a galaxy distance indicator and, once coupled with the galaxy systemic velocity, as a tool to measure the Hubble constant (e.g. Aaronson 1983; Bottinelli, Gougenheim & Teerikorpi 1988; Giovanelli et al. 1997; Sakai et al. 2000; Tutui et al. 2001). Indeed, measuring a characteristic rotation velocity and an apparent luminosity, the TFR-predicted absolute luminosity then yields a distance estimate (e.g. Sandage & Tammann 1976; Bottinelli et al. 1980; Teerikorpi 1987; Fouque et al. 1990; Bureau, Mould & Staveley-Smith 1996; Ekholm et al. 2000). This of course assumes that one knows the mass-to-light ratio and surface density of the object studied, or more commonly that one compares populations of galaxies assumed to have identical  $M/L$  and  $\Sigma$  (e.g. galaxies of a given morphological type at a given epoch).

The TFR implies a tight relationship between luminous mass (traced by  $L$ ) and dynamical or total mass (traced by  $v$ ); evidence that the growths over time of the luminous and dark matter present in galaxies are closely connected. Most importantly, given a reliable measure of distance, the TFR can be turned around and used to probe

\*E-mail: Alfred.Tiley@physics.ox.ac.uk

the mass-to-light ratio and surface density of galaxies. Indeed, many studies have used the zero-point, slope and scatter of the TFR to constrain cosmological models and models of galaxy formation (e.g. Cole & Kaiser 1989; Eisenstein & Loeb 1996; Willick et al. 1997; Steinmetz & Navarro 1999; van den Bosch 2000; Yang, Mo & van den Bosch 2003; Gnedin et al. 2007; McGaugh 2012). In addition, since a galaxy’s redshift is itself a good distance indicator beyond the local Universe, the TFR is a powerful tool to directly probe the evolution of  $M/L$  and  $\Sigma$  over cosmological distances. Our goal here is thus to allow such studies by providing a local TFR benchmark, using molecular gas (CO) as the kinematic tracer.

## 1.2 Immediate motivation

The TFR was originally studied using blue optical rest-frame bands as proxies for the stellar mass of galaxies (see e.g. Tully & Fisher 1977; McGaugh & de Blok 1998; Ziegler et al. 2002). However, these tend to trace young stellar populations and are considerably affected by extinction, resulting in significant intrinsic scatter in the relation (e.g. Verheijen 2001). In recent years and in the present work, near-infrared bands have been utilized instead (see e.g. Conselice et al. 2005; Pizagno et al. 2007; Theureau et al. 2007; Puech et al. 2008), as these suffer little from extinction and better trace the bulk of the stellar mass (e.g. Dickinson et al. 2003), resulting in smaller intrinsic scatter.

Whilst there is a large body of work on the TFR using atomic hydrogen (H I) 21 cm observations (e.g. Tully & Fisher 1977; Sprayberry et al. 1995; Bell & de Jong 2001), there are several advantages to using observations of carbon monoxide (CO), that traces the cold molecular gas in galaxies. First, atomic hydrogen in galaxies is currently only routinely detected in the local Universe. The Square Kilometre Array (SKA) precursors Australian Square Kilometre Array Pathfinder and Karoo Array Telescope (MeerKat) can detect H I to moderate redshifts ( $z \lesssim 0.4$ ; Meyer 2009; Holwerda & Blyth 2010; de Blok 2011; Duffy et al. 2012), but the SKA itself will be required to routinely detect galaxies at  $z > 1$  (Abdalla et al. 2015; Yahya et al. 2015). Multiple transitions of CO are, however, already routinely detected in the bulk of the star-forming galaxy population at  $z \approx 1-3$  (e.g. Daddi et al. 2010; Tacconi et al. 2010, 2013; Magdis et al. 2012; Magnelli et al. 2012; Combes 2013; Freundlich et al. 2013; Genzel et al. 2015), and in star-bursting galaxies up to  $z \approx 7$  (e.g. Walter et al. 2004; Riechers et al. 2008a,b, 2009; Wang et al. 2011; Wagg et al. 2014). CO thus allows us to extend TFR studies probing the mass-to-light ratio and surface density of galaxies to the earliest precursors of today’s galaxies.

Secondly, previous work has shown that the H I discs of galaxies, that are typically more extended spatially than the molecular gas, can also be kinematically unrelaxed, with e.g. large-scale warps (e.g. Verheijen 2001). Molecular gas is generally more dynamically relaxed and suffers less from such problems. More importantly, the atomic hydrogen in early-type galaxies is often significantly disturbed, with much of the gas lying in tidal features or nearby dwarf galaxies (see e.g. Morganti et al. 2006; Serra et al. 2012), thus confusing low-resolution observations such as those obtained with single-dish telescopes. High-resolution interferometric observations are thus necessary to identify those early-type galaxies with a regular H I distribution appropriate to derive reliable TFRs (see e.g. den Heijer et al. 2015). On the other hand, Davis et al. (2011) clearly showed that CO single-dish observations easily yield robust and unbiased TFRs for early-type galaxies. CO observations thus offer the attractive possibility to derive TFRs more accurate

than those currently available, and this across the entire Hubble sequence.

Our goal here is therefore to establish a benchmark CO TFR of local galaxies, as a pre-requisite to extend the relation to higher redshifts. There are clearly tracers other than CO that can be used at large redshifts, primarily optical ionized gas emission lines such as H $\alpha$ , [O II] and [O III], and these should also be pursued to provide independent probes of the evolution of the TFR (see e.g. Cresci et al. 2009; Gnerucci et al. 2011; Miller et al. 2011, 2012). However, it is known that ionized gas discs at  $z \approx 1-3$  are turbulent (see e.g. Förster Schreiber et al. 2006; Swinbank et al. 2012), and great care must be taken when measuring and interpreting their rotational motions (e.g. Wisnioski et al. 2015; Stott et al. 2016; Tiley et al. 2016). With the advent of the Atacama Large Millimeter/submillimeter Array (ALMA),<sup>1</sup> CO emission tracing dynamically cold gas is more easily detectable in high-redshift galaxies than ever before, and embarking on CO TFR studies across the Hubble sequence and redshift is particularly timely.

In this paper, we thus take a step towards establishing a local benchmark for the CO TFR, using the CO(1–0) line as a kinematic tracer. In future work, our TFRs will be compared to those of a local sample (Torii et al., in preparation) and a sample of  $z \lesssim 0.3$  galaxies (Topal et al., in preparation).

The sample, photometric data and kinematic data used in this paper are described in Section 2. TFRs are derived in Section 3 (the rotation velocity measure adopted is defined in Section 3.1 and extensively tested in Appendix A). The results are discussed in Section 4. We summarize and conclude briefly in Section 5.

## 2 DATA

### 2.1 CO velocity widths

As discussed at length in Section 3.1 and Appendix A, we adopt as our TFR velocity measure the width of the integrated CO(1–0) line profile. The GALEX Arecibo SDSS Survey (GASS; Catinella et al. 2010) aimed to observe the neutral hydrogen content of a sample of  $\sim 1000$  galaxies with the Arecibo 305 m telescope. More specifically, GASS galaxies were selected to have redshifts  $0.025 < z < 0.05$ , stellar masses  $10^{10} < M_*/M_\odot < 10^{11.5}$  with a flat distribution in  $\log(M_*/M_\odot)$ , and positions within the overlap region of the Sloan Digitized Sky Survey (SDSS; York et al. 2000), Arecibo Legacy Fast ALFA Survey (ALFALFA; Giovanelli et al. 2005) and GALEX Medium Imaging Survey (Martin et al. 2005; Morrissey et al. 2005). No other selection criterion was applied. A follow-up survey (Catinella, in preparation) has extended the GASS sample to probe down to stellar masses of  $10^9 M_\odot$ . The sample selection and survey strategy are identical to those of the original GASS survey, but for the difference that the lower mass galaxies are selected in the redshift interval  $0.01 < z < 0.02$ .

The CO Legacy Database for GASS (COLD GASS; Saintonge et al. 2011) adds information about the molecular gas contents of a randomly selected sample of 500 GASS galaxies over the full mass range  $10^9 < M_*/M_\odot < 10^{11.5}$ . Most galaxies ( $\approx 80$  per cent) have angular diameters small enough to be observed with a single pointing of the Institut de Radioastronomie Millimétrique (IRAM) 30 m telescope. For larger galaxies, an extra pointing offset from the first was added. Fully reduced and baseline-subtracted integrated CO(1–0) spectra of all massive COLD GASS galaxies ( $M_* > 10^{10} M_\odot$ )

<sup>1</sup> <http://www.almascience.org/>

are publicly available<sup>2</sup> (binned to  $11.5 \text{ km s}^{-1}$  channels), and spectra for the lower mass galaxies have been made available to us ahead of publication. Once combined with other multiband observations, GASS and COLD GASS thus allow us to measure the fraction of the galaxies' baryonic mass contained in atomic gas, molecular gas and stars.

Saintonge et al. define a 'secure' detection in COLD GASS as one with a signal-to-noise ratio  $S/N > 5$ , where  $S/N$  is calculated as the ratio of the integrated line flux to its formal error. Considering the total data set available to us for this work, there are 260 securely detected galaxies. These form the basis of the current sample.

## 2.2 Near-infrared luminosities

Many previous TFR studies have used  $K$ -band magnitudes to probe the bulk of the stellar mass in their sample galaxies. To that end,  $K_s$ -band magnitudes from the Two Micron All Sky Survey (2MASS; Skrutskie et al. 2006) were also considered here, but at the distances of the COLD GASS galaxies, the depth of 2MASS is insufficient to accurately recover  $K_s$ -band magnitudes. Other deeper surveys are available, such as the UK Infrared Telescope Deep Sky Survey (Lawrence et al. 2007), but these tend to have more limited sky coverage.

For this work, the *Wide-Field Infrared Survey Explorer* (WISE; Wright et al. 2010) Band 1 ( $\approx 3.4 \mu\text{m}$ ) magnitude ( $W1$ ) of each sample galaxy was thus adopted as a proxy for its total stellar mass. This quantity is available for 222 of the 260 secure COLD GASS CO detections. Specifically, the magnitude used was the  $w1mag$  parameter from the AllWISE Source Catalogue.<sup>3</sup> This parameter is the  $W1$  magnitude measured in an elliptical aperture, with a size, shape and orientation based on that reported in the 2MASS Extended Source Catalogue (XSC<sup>4</sup>). To account for the larger WISE beam, the aperture is scaled-up accordingly. Those galaxies without an associated  $w1mag$  value are excluded from this work.

It is unclear why 38 of the 260 galaxies securely detected do not have an associated  $w1mag$  value. The 38 galaxies in question are present in the XSC, and the majority of them are also deemed to be extended sources by WISE and are present in the AllWISE Source Catalogue. However, the entries in the latter are not explicitly linked to the corresponding XSC objects despite their close proximity on the sky (typically  $\sim 1$  arcsec). The 38 galaxies do each have a WISE Band 1 magnitude measured in a  $13.75$  arcsec radius aperture ( $\approx 23$  kpc at  $z \approx 0.03$ , the typical redshift of the COLD GASS galaxies),  $w1mag\_4$  from the AllWISE Source Catalogue. To ensure we do not bias our sample by excluding the 38 galaxies in question, we use the available  $w1mag\_4$  values to conduct a Kolmogorov–Smirnov two-sample test between the full 260 securely detected galaxies and the 222 galaxies that remain after the exclusion of the 38 galaxies mentioned. We define a null hypothesis that the  $w1mag\_4$  values of the latter are drawn from the same continuous distribution as those of the former, rejecting the null hypothesis if the  $p$ -value,  $p < 0.05$ . The test produced a  $p$ -value,  $p = 0.68$ , so we cannot reject the null hypothesis. We therefore proceed with our analysis, confident that the exclusion of those 38 galaxies without an associated  $w1mag$  value does not significantly bias the magnitude distribution of our remaining sample.

The bulk of the stellar mass is effectively probed at the wavelength of  $W1$ , but this band is not so far red as to significantly suffer from contamination due to dust emission. In addition, Lagattuta et al. (2013) found that the  $(K - W1)$  colours of a sample of 568 late-type galaxies drawn from the 2MASS Tully–Fisher all-sky galaxy catalogue (Masters, Springob & Huchra 2008) are such that  $(K - W1) \approx 0$  with a scatter of only  $\approx 0.2$  dex. They did find a weak trend towards bluer  $(K - W1)$  colours at  $W1 \geq 10.75$ , but despite this, it is clear that both the  $K$  and  $W1$  bands, with similar wavelength ranges, are tracing the same stellar populations. It is thus acceptable to directly compare TFRs derived using either passband, at least in the regime where differences in depths between surveys is not an issue.

For each sample galaxy, the absolute WISE Band 1 magnitude ( $M_{W1}$ ) was calculated as follows

$$M_{W1} = W1 - A_{3.4\mu\text{m}} - \mu, \quad (2)$$

where  $A_{3.4\mu\text{m}}$  is the extinction in  $W1$ , calculated by first adopting the reddening value  $E(B - V)$  from the dust maps of Schlafly & Finkbeiner (2011) taken from the NASA/IPAC Infrared Science Archive,<sup>5</sup> and converting this to the corresponding  $W1$ -band extinction assuming

$$A_{3.4\mu\text{m}} = R_{3.4\mu\text{m}} E(B - V), \quad (3)$$

where  $R_{3.4\mu\text{m}} = 0.18 \pm 0.1$  was adopted as measured in Yuan, Liu & Xiang (2013) using the stellar 'standard pair' technique. The distance modulus  $\mu$  is taken from the NASA/IPAC Extragalactic Database<sup>6</sup>, and is derived from the galaxy's redshift adjusted for local deviations from the Hubble flow due to the Shapley Cluster, Virgo Cluster and Great Attractor.

Both a reddening and a distance modulus value were available for each of the 222 remaining galaxies.

## 2.3 Inclination estimates

To account for projection effects, each sample galaxy's inclination  $i$  was calculated as

$$\cos(i) = \left( \frac{q^2 - q_0^2}{1 - q_0^2} \right)^{1/2}, \quad (4)$$

where  $q$  is the observed ratio of the semiminor to the semimajor axis of the galaxy in SDSS  $r$ -band imaging, available for 217 of the 222 remaining sample galaxies. Those galaxies without an associated  $q$  value are excluded from this work. The (intrinsic) axial ratio of an edge-on galaxy,  $q_0$ , is morphology dependent. We adopt the same prescription as Davis et al. (2011), whereby galaxies are divided into early types with  $q_0 = 0.34$  and late types with  $q_0 = 0.2$ . See Section 2.6 for a description of the morphological classifications used.

## 2.4 Stellar masses

The stellar masses of our sample galaxies were taken from the Max Planck Institute for Astrophysics-Johns Hopkins University Data Release 7 derived data catalogue,<sup>7</sup> and were determined using SDSS photometry via the spectral energy distribution (SED)-fitting method described by Salim et al. (2007), assuming a Chabrier (2003)

<sup>2</sup> [http://www.mpa-garching.mpg.de/COLD\\_GASS/](http://www.mpa-garching.mpg.de/COLD_GASS/)

<sup>3</sup> <http://wise2.ipac.caltech.edu/docs/release/allwise/>

<sup>4</sup> <http://irsa.ipac.caltech.edu/applications/2MASS/PubGalPS/>

<sup>5</sup> <http://irsa.ipac.caltech.edu/applications/DUST/>

<sup>6</sup> <http://ned.ipac.caltech.edu/>

<sup>7</sup> <http://www.mpa-garching.mpg.de/SDSS/DR7/>

initial mass function (IMF). In this method, each galaxy’s SED is compared to model SEDs from the library of Bruzual & Charlot (2003) to determine a stellar mass probability distribution. The stellar mass and its uncertainty are then taken as the median and half the difference between the 16th and 84th percentile of this distribution, respectively, and are available for 216 of the 217 remaining sample galaxies. The single galaxy without an associated stellar mass value is excluded from this work.

## 2.5 AGN candidates

As the emission from an active galactic nucleus (AGN) can contaminate and occasionally far outweigh that of the stellar body of a galaxy, it is imperative to exclude from our sample galaxies hosting a substantial AGN. AGN-hosting galaxies would otherwise be systematically offset from the underlying TFR and would systematically bias our fits.

We used publicly available classifications from the *emission-LinesPort* table of the SDSS Data Release 10<sup>8</sup> to exclude AGN-candidates from our sample. Each SDSS galaxy was classified by a fit to its spectrum using adaptations of the Gas AND Absorption Line Fitting (GANDALF; Sarzi et al. 2006) and penalized PiXel Fitting (PPXF; Cappellari & Emsellem 2004) routines to extract several emission lines. These were then used to place each galaxy on a Baldwin, Phillips & Terlevich (Baldwin, Phillips & Terlevich 1981) diagram. Based on their position on the diagram, galaxies were divided into different categories that depend on the likelihood of the galaxy hosting an AGN. The classifications themselves are based on the work of Kauffmann et al. (2003), Kewley et al. (2001) and Schawinski et al. (2007). We thus excluded nine galaxies classified as ‘Seyfert’, further reducing our adopted sample to 207 galaxies.

## 2.6 Morphological classes

Our COLD GASS sample was cross-referenced with the Galaxy Zoo 1 catalogue (GZ1; see Lintott et al. 2008, 2011), providing crowd-sourced classifications of ~600 000 galaxies in the SDSS. Each galaxy is classified as either a spiral, an elliptical or ‘uncertain’. Of our remaining sample of 207 galaxies drawn from COLD GASS, 143 are deemed to be spirals, 6 ellipticals and the remaining 58 are uncertain. For the purposes of this work, and in particular, the inclination correction described in Section 2.3, we equate those galaxies classified as spiral and uncertain to late types, and those classified as elliptical to early types.

We do not initially exclude any galaxy based on its GZ1 morphological classification. However, the exclusion (or inclusion) of those galaxies deemed elliptical or uncertain is discussed further in Section 3.3, where we present the details of a more restricted sub-sample.

After applying all the criteria described in this section, we thus proceed with a final working sample of 207 COLD GASS galaxies.

## 3 COLD GASS TFRs

### 3.1 Measuring $W_{50}$

As a characteristic velocity measure, we adopt  $W_{50}$ , the width of the CO(1–0) integrated profile at 50 per cent of its maximum, that should be roughly equal to twice the maximum rotation velocity

of the galaxy  $V_{\max}$ . In the presence of non-negligible noise, a fit to the profile is usually superior to a direct measurement of  $W_{50}$ , but the choice of the fitting function is not trivial and several different functions have been used in the past.

While it is expected that the characteristic velocity measure will vary depending on the function chosen, this is acceptable as long as different galaxy samples being compared are measured in the same manner. This is because the systematic effect introduced by any given function will cancel out when the difference between two (or more) samples is calculated. However, it is clearly preferable for the measured characteristic velocity to be independent of the signal to noise and amplitude-to-noise ratio ( $A/N$ ) of the data, and the measurements should not be systematically biased as the width and/or shape of the profile vary. Despite previous work on the subject (e.g. Saintonge 2007; Obreschkow et al. 2009a,b; Westmeier et al. 2014), as the signal-to-noise ratio of CO data is generally low (certainly lower than that of typical H I spectra of nearby galaxies; e.g. Lavezzi & Dickey 1998), we deemed it prudent to compare the results of several different fitting functions.

This comparison is described in detail in Appendix A, where we conclude that the Gaussian Double Peak function (equation A2) is the most accurate and minimises potential biases as a function of  $A/N$ , inclination (apparent width) and rotation velocity (intrinsic width). We therefore deem it the most appropriate function with which to measure the CO(1–0) linewidths of the COLD GASS galaxies, and adopt it throughout this work.

The CO velocity width ( $W_{50}$ ) of every sample galaxy was thus measured by fitting the Gaussian Double Peak function to its observed integrated CO(1–0) spectrum from COLD GASS, this using the Levenberg–Marquardt algorithm to minimize the reduced  $\chi^2$ , given by

$$\chi_{\text{red}}^2 \equiv \left( \sum_i \frac{[F(v_i) - f(v_i)]^2}{\sigma_{\text{rms}}^2} \right) / \text{DOF}, \quad (5)$$

where  $F(v_i)$  is the observed CO(1–0) spectrum flux density in velocity bin  $v_i$ ,  $f(v_i)$  is the model flux density in that same velocity bin from the Gaussian Double Peak function (i.e. the integral of the function across the bin divided by the bin width),  $\sigma_{\text{rms}}$  is the root mean square (rms) noise of the spectrum measured in a spectral range devoid of signal, DOF is the number of degrees of freedom associated with the fit, and the sum is taken over all velocity bins  $v_i$  of the spectrum. The best fits overlaid on the observed spectra are shown in Appendix C for all galaxies in our final sub-sample (see Section 3.3).

Despite the fact that the Gaussian Double Peak function proved to be the most robust function for fitting the CO profiles, this function reduces to a single Gaussian in the limit where the half-width of the central parabola  $w \rightarrow 0$  (see equation A2). As  $w > 0$  was the only condition imposed on  $w$  during the Gaussian Double Peak function fitting process, there are cases where the best-fitting value of  $w$  is less than the spectra’s 11.5 km s<sup>−1</sup> velocity bin width. In these cases, it is thus clear that a single Gaussian would be a more natural (and perhaps better) fit.

With this in mind, a strategy was adopted whereby each galaxy spectrum was fit with both the Gaussian Double Peak function and a standard Gaussian (see equation A1). The value of  $|1 - \chi_{\text{red}}^2|$  for each function was then calculated and the two values compared. The fit with the smallest value was then adopted in each case.

One further caveat was necessary, since in some cases the best fit for the Gaussian Double Peak function resulted in the peak of the central quadratic  $A_C$  (i.e. the central flux) being significantly greater

<sup>8</sup> <http://skyserver.sdss.org/dr10>

than the peak values of the flanking Gaussians  $A_G$ . In these cases, the central quadratic has a convex rather than a concave or flat shape (as may be expected for respectively a double-horned or boxy-shaped profile). In these cases, specifically those for which  $A_C > (3/2)A_G$ , it was thus again deemed more appropriate to adopt the best-fitting Gaussian rather than the Gaussian Double Peak function.

Finally, for each spectrum,  $\text{MPFIT}$  was used to explore the parameter space to find the combination of parameters that best fit the data. The best fit that  $\text{MPFIT}$  returns can be sensitive to the user-supplied initial guesses as local minima in the  $\chi^2$  space can be mistaken for the global minimum by the fitting process. To reduce the chance of converging on a local minimum, and therefore not finding the true best-fitting parameters,  $\text{MPFIT}$  was run several times for each spectrum, each time with a different set of initial guesses. The run with the smallest  $|1 - \chi_{\text{red}}^2|$  value was then adopted as the best fit. The velocity width of the Gaussian Double Peak function at 50 per cent of the peak,  $W_{50}$ , was then calculated in an analytical manner:

$$W_{50} = 2(w + \sigma \sqrt{2 \times \ln(2)}). \quad (6)$$

The same applies to the pure Gaussian function with  $w = 0$ .

The velocity width uncertainty,  $\Delta W_{50}$ , was then estimated by generating 150 realizations of the best-fitting model, each with random Gaussian noise  $\sigma_{\text{rms}}$  added. Each realization was fit as described above and  $\Delta W_{50}$  taken as the standard deviation of the velocity width distribution.

### 3.2 Fitting the TFRs

Both a forward and a reverse straight line fit was made to each of the resulting TFRs using a Levenberg–Marquardt minimization technique, again with  $\text{MPFIT}$ . The familiar forward fit minimizes

$$\chi_{\text{for}}^2 \equiv \sum_i \left( \frac{1}{\sigma_i^2} \right) \{y_i - [m(x_i - x_0) + b]\}^2, \quad (7)$$

where  $x_i$  and  $y_i$  are, respectively, the velocity and flux datum,  $x_0$  is a ‘pivot’ point chosen to minimize the uncertainty in the straight line intercept  $b$  (in practice, we set  $x_0$  to the median value of the  $x_i$ ),  $m$  is the straight line gradient, and the sum is over all sample galaxies.  $\sigma_i$  is defined as

$$\sigma_i^2 \equiv \sigma_{y,i}^2 + m^2 \sigma_{x,i}^2 + \sigma_{\text{int}}^2, \quad (8)$$

where  $\sigma_{y,i}$  and  $\sigma_{x,i}$  are, respectively, the uncertainty of an individual data point in  $y$  and  $x$ , and  $\sigma_{\text{int}}$  is a measure of the intrinsic scatter in the TFR, determined by adjusting its value such that  $\chi_{\text{for}}^2/\text{DOF} = 1$ .

The total scatter in the relation is then

$$\sigma_{\text{tot}}^2 = \frac{\chi_{\text{for}}^2}{\sum_i (1/\sigma_i^2)}. \quad (9)$$

For the reverse fit, the figure of merit to minimize is

$$\chi_{\text{rev}}^2 = \sum_i \left( \frac{1}{\zeta_i^2} \right) [x_i - (M y_i + B + x_0)]^2, \quad (10)$$

where similarly  $M$  and  $B$  are, respectively, the gradient and intercept of the straight line and

$$\zeta_i^2 \equiv \sigma_{x,i}^2 + M^2 \sigma_{y,i}^2 + \zeta_{\text{int}}^2. \quad (11)$$

$\zeta_{\text{int}}$  is again the intrinsic scatter, determined such that  $\chi_{\text{rev}}^2/\text{DOF} = 1$ . The total scatter is then

$$\zeta_{\text{tot}}^2 = \frac{\chi_{\text{rev}}^2}{\sum_i (1/\zeta_i^2)}. \quad (12)$$

The reverse fit parameters can be directly compared to the forward fit parameters by defining the equivalent slope, intercept, intrinsic scatter and total scatter as  $m' \equiv 1/M$ ,  $b' \equiv -B/M$ ,  $\sigma'_{\text{int}} \equiv M \zeta_{\text{int}}$  and  $\sigma'_{\text{tot}} \equiv M \zeta_{\text{tot}}$ , respectively (Williams, Bureau & Cappellari 2010).

### 3.3 Defining a sub-sample

As described in Section 2, an initial sample was drawn from the COLD GASS data that contains all galaxies with a secure CO(1–0) detection, *WISE* W1 photometry, an SDSS  $r$ -band axial ratio, a stellar mass via multiband photometry, no AGN, and a GZ morphological classification for a total of 207 galaxies. The W1-band and stellar mass TFRs for this initial sample are shown in Figs 1(a) and 2(a), respectively, and the fit parameters are listed in Tables 1 and 2, respectively. Clearly, for both the W1-band and stellar mass TFRs, the intrinsic and total scatters are very large for this initial sample.

There are several factors contributing to the observed scatter. First, as shown in Fig. A4, the measured velocity widths of nearby face-on galaxies are unreliable, in the sense that they do not accurately reproduce the intrinsic widths and their fractional errors are dependent on those widths. We thus removed from the initial sample galaxies with an inclination  $i < 30^\circ$ , resulting in a sub-sample of 180 galaxies.

Secondly, one must gauge whether the CO extends to sufficiently large radii to sample the flat part of the galaxies’ rotation curves. This is essential, as otherwise the measured velocity widths will not be representative of the total dynamical masses, introducing additional scatter in the relations. Although not necessary, empirical studies have shown that the kinematic tracer of galaxies with a boxy or double-horned integrated profile usually extends beyond the turnover of the rotation curve (e.g. Davis et al. 2011). A Gaussian profile may imply that insufficient CO is present in the outer parts to robustly recover the flat part of the rotation curve, or that the rotation curve itself is not flat. Of course, a Gaussian profile can also arise, despite sufficient CO present in the outer parts of a galaxy, if there is a particularly high concentration of gas in the central regions of the galaxy (e.g. Lavezzi & Dickey 1997; Wiklind et al. 1997), but this is a risk worth taking. Lastly, given the finite width of the velocity channels, rejecting profiles that do not appear boxy or double-horned may also exclude profiles that are intrinsically boxy or double-horned but simply have small linewidths, an effect that would preferentially affect the low-mass end of the TFRs. However, this drawback is small compared to the benefits of significantly reduced scatter.

This approach is consistent with the understanding that the flat part of a galaxy’s rotation curve is accurately recovered, provided that the ‘flaring parameter’ of the integrated profile (i.e. the ratio of the linewidth at 20 per cent of the peak flux to that at 50 per cent) is less than  $\approx 1.2$  (Lavezzi & Dickey 1997, 1998). In other words, both methods select integrated profiles with steep edges. We therefore reduced our sample further by requiring that the integrated CO(1–0) profile of each galaxy be either boxy or double-horned. In practice, this amounts to excluding galaxies whose profile was best fit by a single Gaussian function rather than the Gaussian Double Peak function, resulting in a sub-sample of 94 galaxies.

Thirdly, we consider how well our line profile fits recover the true velocity widths at small amplitude-to-noise ratios,  $A/N$ . As illustrated in Fig. A1,  $A/N \geq 1.5$  is generally required to recover the true velocity width to 10 per cent or better. Given the limited size of the COLD GASS sample and the typical quality of the CO data,

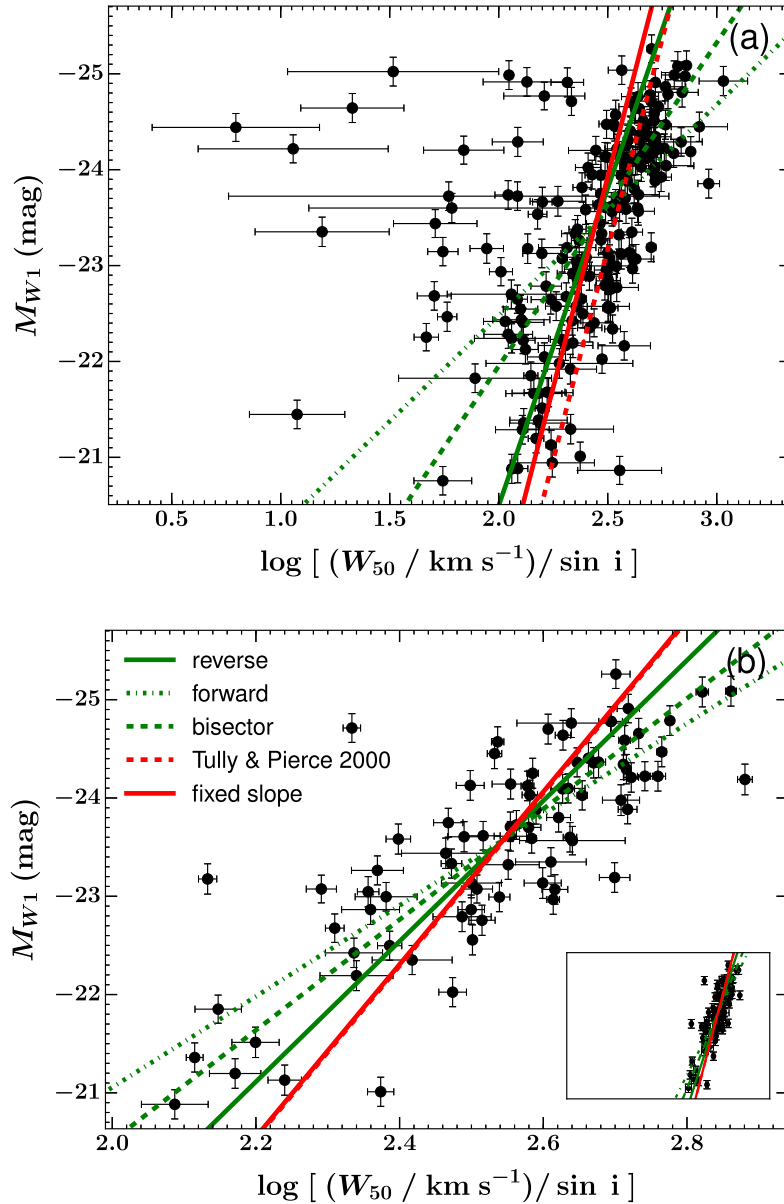


**Figure 1.** COLD GASS W1-band Tully–Fisher relations. (a) and (b) show the TFR for the initial COLD GASS sample and our final sub-sample, respectively. The  $x$ -axis is the width of the integrated CO(1–0) profile at 50 per cent of the peak, corrected for the effect of inclination. The  $y$ -axis is the absolute *WISE* Band 1 magnitude  $W_1$  ( $\approx 3.4 \mu\text{m}$ ). The green dot–dashed, solid and dashed lines show the forward fit, reverse fit, and the bisector of the two, respectively. The dashed red line is the  $K$ -band TFR of Tully & Pierce (2000). The solid red line shows the best fit when the gradient is constrained to that of Tully & Pierce. To demonstrate the reduction in scatter between the initial and final sub-sample, the embedded panel in (b) shows the TFR for the final sub-sample but over the same axis ranges as (a).

this threshold also ensures a final sub-sample with a sufficiently large number of galaxies for robust TFR fits. Applying this  $A/N$  cut results in a sub-sample of 88 galaxies.

Fourthly, to have confidence in the accuracy of the velocity widths derived from the profile fits, we remove those galaxies with a fractional uncertainty  $\Delta W_{50}/W_{50} > 20$  per cent. This further reduces our sub-sample to 84 galaxies.

Lastly, we consider the morphologies of our sample galaxies, as galaxies of different morphological types have different TFR zero-points (presumably due to different surface mass densities and mass-to-light ratios; see equation 1). In particular, there is a clear offset between early- and late-type galaxies (see e.g. Williams et al. 2010; Davis et al. 2011). In fact, the work of Davis et al. (2016)

suggests that very massive early-type galaxies are again offset from the TFR of early types of lower masses. There are also possible variations of the TFR slope among late-type galaxies (e.g. Lagattuta et al. 2013).

Fig. 3 shows the TFR of our galaxy sub-sample after all the aforementioned cuts have been applied, and where all galaxies have been labelled according to their morphological type (see Section 2.6). Error bars have been omitted for clarity. As there is only one early-type galaxy, it was removed from the sub-sample. As the galaxies of uncertain morphological type are essentially indistinguishable from the late types, with a similar slope, zero-point and scatter, there is no reason to exclude them and we instead assimilate them to the late-type galaxies.

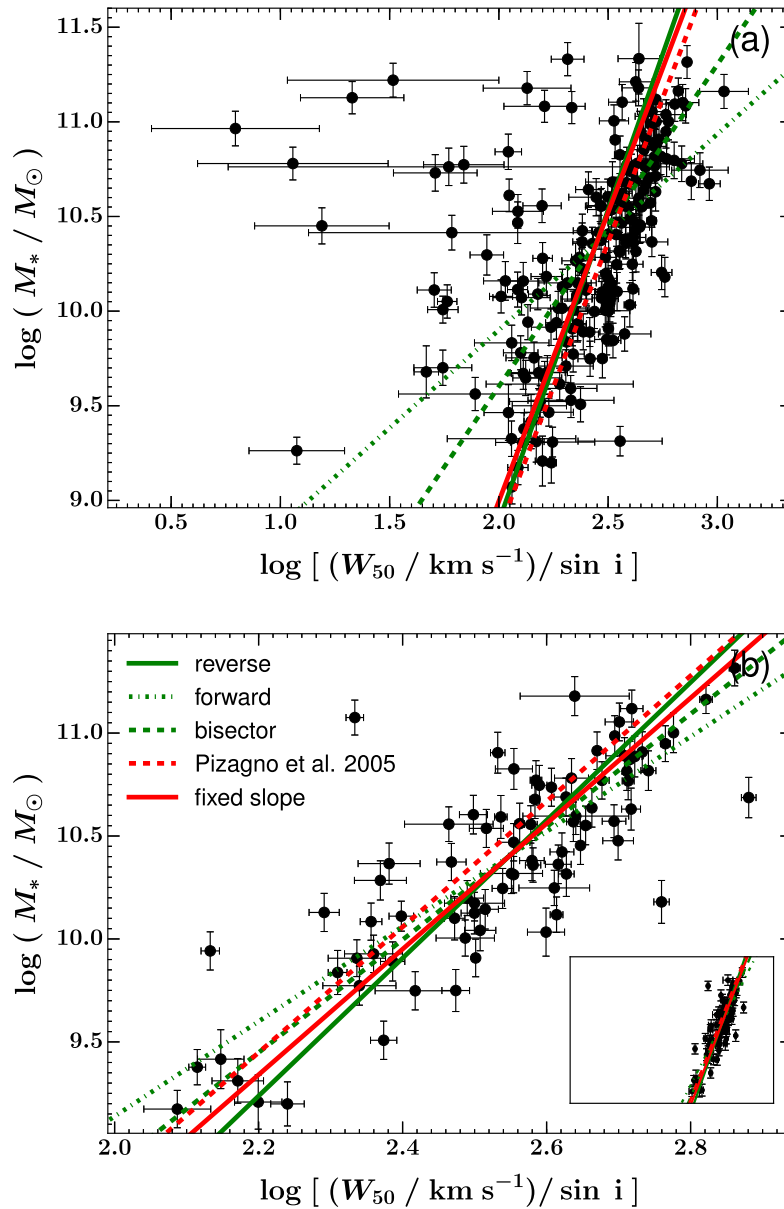


**Figure 2.** As Fig. 1, but for the COLD GASS stellar mass Tully–Fisher relations. The dashed red line is the stellar mass TFR of Pizagno et al. (2005). The solid red line shows the best fit when the gradient is constrained to that of Pizagno et al.

**Table 1.** Parameters of the  $W1$ -band Tully–Fisher relations.

Sample	Pivot	Fit	Slope	Intercept (mag)	Intrinsic scatter (mag)	Total scatter (mag)	Offset (mag)
Initial	2.49	Forward	$-2.2 \pm 0.3$	$-23.56 \pm 0.07$	$0.92 \pm 0.05$	$0.95 \pm 0.02$	–
		Reverse	$-6.6 \pm 0.7$	$-23.7 \pm 0.1$	$1.5 \pm 0.1$	$1.62 \pm 0.01$	–
		Bisector	$-3.4 \pm 0.3$	$-23.60 \pm 0.01$	–	–	–
		Fixed	$-8.78$	$-23.8 \pm 0.1$	$2.0 \pm 0.1$	$2.18 \pm 0.01$	$-0.8 \pm 0.2$
Sub-sample	2.58	Forward	$-4.6 \pm 0.4$	$-23.74 \pm 0.07$	$0.59 \pm 0.05$	$0.61 \pm 0.01$	–
		Reverse	$-7.1 \pm 0.6$	$-23.83 \pm 0.09$	$0.73 \pm 0.06$	$0.76 \pm 0.01$	–
		Bisector	$-5.6 \pm 0.3$	$-23.77 \pm 0.01$	–	–	–
		Fixed	$-8.78$	$-23.9 \pm 0.1$	$0.94 \pm 0.08$	$0.96 \pm 0.01$	$0.0 \pm 0.1$

Overall, this thus leads to a final sub-sample comprising 83 late-type galaxies, that we use for both  $W1$ -band and stellar mass TFR fits. The resulting  $W1$ -band and stellar mass TFRs for this final sub-sample are shown in Figs 1(b) and 2(b), respectively, while the fit

parameters are listed in Tables 1 and 2, respectively. As desired, the observed scatters of our final sub-sample are significantly reduced compared to those of the initial sample, this for both the  $W1$ -band and stellar mass TFR.

**Table 2.** Parameters of the stellar mass Tully–Fisher relations.

Sample	Pivot	Fit	Slope	Intercept (dex)	Intrinsic scatter (dex)	Total scatter (dex)	Offset (dex)
Initial	2.49	Forward	$1.0 \pm 0.1$	$10.41 \pm 0.03$	$0.44 \pm 0.03$	$0.47 \pm 0.01$	–
		Reverse	$3.3 \pm 0.4$	$10.50 \pm 0.06$	$0.77 \pm 0.05$	$0.824 \pm 0.004$	–
		Bisector	$1.7 \pm 0.1$	$10.44 \pm 0.01$	–	–	–
		Fixed	3.05	$10.49 \pm 0.05$	$0.73 \pm 0.05$	$0.765 \pm 0.003$	$0.16 \pm 0.06$
Sub-sample	2.58	Forward	$2.3 \pm 0.2$	$10.48 \pm 0.03$	$0.27 \pm 0.02$	$0.287 \pm 0.004$	–
		Reverse	$3.3 \pm 0.3$	$10.51 \pm 0.04$	$0.32 \pm 0.03$	$0.344 \pm 0.005$	–
		Bisector	$2.7 \pm 0.2$	$10.49 \pm 0.01$	–	–	–
		Fixed	3.05	$10.50 \pm 0.03$	$0.30 \pm 0.03$	$0.318 \pm 0.003$	$-0.11 \pm 0.04$

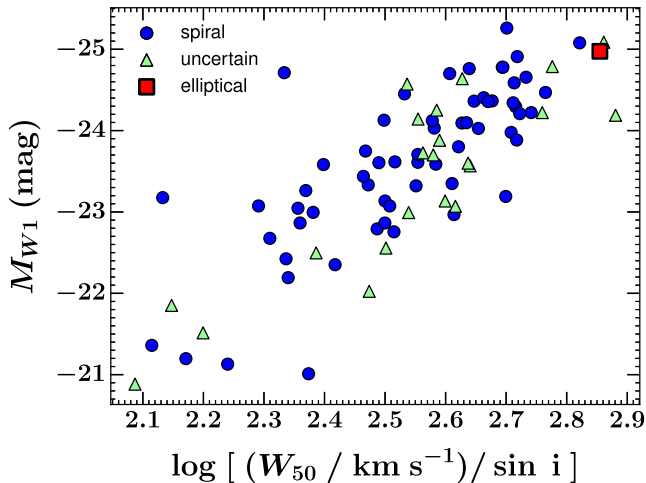


**Figure 3.** As Fig. 1, but for an intermediate (although nearly final) COLD GASS sub-sample (as described in Section 3.3). Error bars are omitted for clarity and the galaxies are identified by their GZ1 morphological type (see Section 2.6): blue circles for spirals (late types), red squares for ellipticals (early types), and green triangles for uncertain types. It is clear that those galaxies deemed uncertain follow broadly the same relation as, and do not exhibit increased scatter in comparison to, those deemed spirals.

### 3.4 The TFRs

As described above, Figs 1 and 2 show the COLD GASS  $W1$ -band and stellar mass TFR, respectively, for both the initial and final sub-samples, with the forward, reverse and bisector fits overlaid. Tables 1 and 2 list the corresponding fit parameters. The reverse fit parameters have been adjusted to be directly comparable to the forward fit parameters, as described in Section 3.2.

A comparison relation is also displayed on each plot: for the  $W1$ -band TFR, the  $K$ -band relation of Tully & Pierce (2000), who used  $H\text{ I}$  integrated profiles to measure the galaxy rotation velocities; for the stellar mass TFR, the stellar mass relation of Pizagno et al. (2005), who used long-slit observations of  $H\alpha$  emission to measure the ionized gas rotation. Based on the work of Madau & Dickinson (2014), we apply a small offset in  $\log(M_*/M_\odot)$  of  $-0.034$  dex to the latter, to convert from a Kroupa (Kroupa 2001) to a Chabrier IMF. A fit to the COLD GASS data with the slope fixed to that of the comparison relation is also shown in each case, allowing us to gauge any offset between the comparison and COLD GASS samples. We recall that with  $(K - W1) \approx 0 \pm 0.2$  for late-type galaxies, a  $W1$ – $K$  comparison is justified (Lagattuta et al. 2013).

As expected, the reverse fits are always much steeper than the forward fits, and indeed for both initial and final sub-samples and

$W1$ -band and stellar mass TFRs, the slopes of the reverse fits are much closer to those of the comparison samples.

It is well established that a significant bias in the slope is introduced by using a forward fit (e.g. Schechter 1980; Teerikorpi 1987; Sandage 1988; Tully & Pierce 2000; Tully & Courtois 2012; Sorce et al. 2013), stemming from the selection criteria imposed on galaxy samples used in TFR studies. This bias is explained in detail by Willick (1994).

To understand why this approach is problematic, first consider the measured TFR of a complete (i.e. independent of any selection) sample of galaxies, with some Gaussian intrinsic scatter in magnitude (and indeed linewidth). For a given linewidth, a galaxy may be scattered either above or below the TFR if it is intrinsically brighter or dimmer than the corresponding mean magnitude for that linewidth (i.e. that predicted by the true, unbiased TFR). Now consider measuring the TFR for the same sample but for the common case where a limiting magnitude is imposed, such that galaxies dimmer than the limiting value are excluded from the analysis. At the faint end of the TFR, those galaxies that are intrinsically brighter than the mean will be preferentially included in the analysis, whilst those that are dimmer will be excluded. This acts to flatten the slope of the measured TFR as, at the small line-width end, the sample is biased brighter than the true underlying distribution. This bias is compounded by the fact that the uncertainties in the line-width measurements are typically at least comparable (and often larger) than those in the luminosity measurements.

Since in this scenario there is no selection via linewidth, the reverse fit, which minimizes the residuals in linewidth, avoids this bias. Willick (1994) points out that, in practice, some bias will still remain for the reverse fit when considering the TFR in a waveband other than that used to select the sample. This is particularly relevant to this work, since the GASS sample (and therefore COLD GASS) was not selected via a limiting  $W1$  magnitude but was rather selected to be flat in  $\log(M_*/M_\odot)$  above a minimum stellar mass value (see Section 2.1). Nevertheless, the bias in the reverse fit is much reduced compared to that of the forward fit. Willick et al. (1995), for example, find a reduction of a factor of 6 in the bias between the forward and reverse fit when examining the TFRs of several samples of spiral galaxies selected in the  $I$  and  $r$  bands. In light of this, the parameters in this work derived from a forward fit should be treated with a degree of caution.

As desired, following the exclusion of potential sources of scatter (see Section 3.3), for both the  $W1$ -band and the stellar mass TFR, there is a much greater scatter in the initial sample than in the final sub-sample. In addition, the intrinsic and total scatters are always larger in the reverse fit than in the forward fit, reflecting the larger scatter in  $W_{50}$  than in  $M_{W1}$  and  $M_*$ .



## 4 DISCUSSION

### 4.1 Slope

Treating the forward fits with suspicion, it is most sensible to compare the results of previous studies to the reverse fits only. The unconstrained reverse fit to the *W1* TFR is shallower than the relation found by Tully & Pierce (2000) for both the initial and final sub-sample, even allowing for the uncertainties (although Tully & Pierce do not quote an uncertainty on their slope). However, the slope of both sub-sample's stellar mass TFR agrees with that of the Pizagno et al. (2005) TFR, after allowing for uncertainties (Pizagno et al. 2005 quote an uncertainty of  $\pm 0.12$  on their slope). The stellar masses are model dependent, however, so the significance of this result is uncertain, particularly given the comparatively shallower slope of the *W1* relation.

Several factors could of course affect the slope of the COLD GASS TFRs, in particular, a potential Malmquist bias and the fact that galaxies of various primarily late-type morphologies were amalgamated together. The former factor is likely to be most acute for the stellar mass TFRs, as the COLD GASS sample was stellar mass-selected, but it is unlikely to be important for the final sub-sample as our various selection criteria, in particular, the integrated profile shape criterion (see Section 3.3), have largely washed out any abrupt stellar mass threshold. Of course the same criterion may also preferentially exclude those galaxies with small linewidths. However, this effect is likely to be small in comparison to the Malmquist bias introduced via the GASS (and thus COLD GASS) selection function. The latter factor is undoubtedly present to some extent, but it is hard to quantify without better morphologies. Indeed, as our samples contain a variety of (mainly late-type) galaxy morphologies, and the slope of the TFR varies with galaxy type, the measured slopes are effectively averages of multiple slopes for different galaxy morphologies.

Lastly, we must also consider whether the very use of CO as a kinematic tracer may bias the slope of the TFR, such that the resultant slope is shallower than that of the  $H\ I$  TFR of the same sample. Indeed, the linewidths of Tully & Pierce (2000) are measured from  $H\ I$  observations, whereas the COLD GASS linewidths are measured from CO(1–0). In Appendix B, for subsets of COLD GASS galaxies with both CO(1–0) and  $H\ I$  data, we compare the values of  $W_{50}$  as derived from the width of both the CO(1–0) and  $H\ I$  integrated profiles (as described in Section 3.1). We find that the slope of the TFRs constructed using CO(1–0) are either comparable to or slightly shallower than those of the  $H\ I$  TFRs of the same galaxies. However, the slopes of both the CO(1–0) and  $H\ I$  TFRs agree within uncertainties. We may therefore cautiously attribute some of the difference in slope between the COLD GASS *W1* TFR and the comparison relation to the use of CO(1–0) (rather than  $H\ I$ ) as a kinematic tracer, but it should be stressed that, on the basis of the comparison in Appendix B, this is not likely to be the driving factor of the difference. Furthermore, as shown again in Appendix B, much is to be gained from using CO rather than  $H\ I$ , as it leads to much smaller intrinsic (and thus total) scatter for the sub-sample.

### 4.2 Inclinations

The uncertainties on the measured inclinations  $i$  contribute greatly to the uncertainties on the inclination-corrected velocity widths  $W_{50}/\sin i$ , particularly at small inclinations (and even with an  $i > 30^\circ$  threshold). The robustness of any constructed TFR is thus highly dependent on the accuracy of the inclination measurements. The scat-

ter of the TFR is likely to increase with decreasing accuracy, with possibly a smaller systematic effect affecting the measured slope.

The axial ratio method used in this work is appropriate for the relatively shallow ground-based optical imaging used, but it is not particularly refined. First, it naively assumes that galaxies can be grouped into categories sharing a unique edge-on (intrinsic) axial ratio (here 0.2 and 0.34 for late types and early types, respectively). The morphologies of galaxies are, in reality, much more diverse, and the intrinsic axial ratio is likely to vary within any defined category. This is particularly relevant to our work, as the inclination measurements are ultimately dependent on the relatively crude GZI morphological classifications. Davis et al. (2011), in fact, showed that the scatter in the TFR of a sample of early-type galaxies is reduced when one uses a measure of inclination derived from the intrinsically very flat dust features visible in high-resolution (*Hubble Space Telescope*) imaging, rather than stellar light as used here. While the magnitude of the effect was certainly amplified by the use of early-type galaxies, it nevertheless illustrates the point.

Having said that, as our inclinations are based on rather shallow ground-based imaging, it may also be that they are systematically underestimated (the galaxies appearing rounder than they really should), leading to overestimated inclination corrections to the velocity widths. As this effect is likely to be more acute in smaller, lower mass galaxies, however, it would lead to steeper rather than shallower TFRs.

### 4.3 Offset

We measure a small offset between the stellar mass TFR for both the initial and final sub-samples presented in this work and that of Pizagno et al. (2005) ( $+0.16 \pm 0.06$  and  $-0.11 \pm 0.04$  dex, respectively). Considering the *W1*-band TFRs, we measure a large negative offset ( $-0.8 \pm 0.2$  mag) between the initial sample's TFR and that of Tully & Pierce (2000). However, this offset disappears when considering the (more reliable) *W1*-band TFR for the final sub-sample. Importantly, in all cases, the offset between the COLD GASS and the comparison sample TFR (at fixed slope) is much smaller than the intrinsic scatter. There is thus no evidence for any significant offset between the COLD GASS and comparison samples, as expected given the similar redshifts and morphologies of the samples' galaxies.

### 4.4 Scatter

The intrinsic and total scatters of the *W1*-band TFR for our final sub-sample, for the forward unconstrained fit, were found to be  $0.59 \pm 0.05$  and  $0.61 \pm 0.01$  mag, respectively. These values are slightly larger than those of previous near-infrared TFR studies. Tully & Pierce (2000) found a  $K'$ -band total rms scatter of 0.44 mag for local spiral galaxies, whilst Verheijen (2001) found a 0.32 mag total scatter for the same passband. However, Pizagno et al. (2007) found an intrinsic scatter of 0.42–0.46 mag across the  $g$ ,  $r$ ,  $i$  and  $z$  bands.

Considering the stellar mass TFR of the final sub-sample, the intrinsic and total scatters of the forward unconstrained fit were found to be  $0.27 \pm 0.02$  and  $0.287 \pm 0.004$  dex, respectively. As with the *W1*-band relation, this is larger than previous TFR studies in the local Universe. Bell & de Jong (2001) found a total scatter of just 0.13 dex, whilst Pizagno et al. (2005) similarly found an intrinsic scatter of 0.16 dex.

The reasons why we measure a slightly higher intrinsic scatter than previous studies are unclear. In Appendix B, we show that the use of linewidths derived from CO(1–0) integrated profiles leads to

increased scatter in the TFR, compared to the same TFR constructed using H I integrated profiles. However, this difference in scatter disappears when we apply the criteria used to select the sub-sample described in Section 3.3. This implies that the increased scatter is due to the inclusion of CO(1-0) profiles that do not display a boxy or double-horned shape. Once these systems are removed, the intrinsic and total scatter of the CO(1-0) TFRs are actually less than those of the H I TFRs for the same galaxies.

As discussed above, the mix of several different late-type morphologies may affect the slope and scatter (through different mass surface densities  $\Sigma$  and mass-to-light ratios  $M/L$ ; see Section 1.1), while our inclinations may be underestimated. While we have taken great care to estimate and propagate uncertainties on our measurements, it may also be that our observational errors are underestimated (leading to an overestimate of the intrinsic scatter). The uncertainties on the stellar masses and inclinations are particularly hard to reliably estimate.

#### 4.5 Sample selection

The selection criteria of GASS, and thus COLD GASS, present two potential problems when using galaxies drawn from these samples to build TFRs. The first, discussed at length above, is the problem of fitting a single TFR (slope and zero-point) to a sample of galaxies with differing morphologies. The second is that both the GASS and COLD GASS samples are chosen to be flat in  $\log M_*$ . This means that, compared to e.g. a volume- or flux-limited sample, galaxies of large masses will be overrepresented. This could result in an inferred TFR with a shallower than expected slope, depending on how heavily weighted high-mass galaxies are in comparison to low-mass galaxies.

The sub-sample selection, as described in Section 3.3, leads to a dramatic and significant reduction in the scatter of the TFRs. The main driver in this reduction is the exclusion of galaxies with profiles that do not appear boxy or double-horned. This ensures that we include in our analysis only those galaxies with sufficient CO in the outer parts to properly sample the flat parts of the rotation curve. This is at the expense of the possible rejection of profiles that are intrinsically boxy or double-horned but simply appear Gaussian due to their small linewidth and the finite width of the velocity channels. This cut by profile shape preferentially affects the low-mass end of the TFRs, and could therefore bias their resultant slopes. However, the effect is likely to be small (and opposite to the Malmquist bias) and the benefits of the significantly reduced scatter far outweigh the drawbacks.

## 5 CONCLUSIONS AND FUTURE WORK

In an effort to firmly establish the CO TFR as a useful tool to probe the evolution of galaxies over cosmic time, we first tested the self-consistency and robustness of four functions appropriate to fit the integrated line profiles of galaxies, particularly in the low signal-to-noise ratio regime characteristic of molecular gas observations. The Gaussian Double Peak function was deemed to be the most self-consistent and to suffer the least from possible systematic biases as a function of the amplitude-over-noise ratio  $A/N$ , the galaxy inclination  $i$  and the intrinsic flat circular velocity  $V_{c, \text{flat}}$ .

We then constructed the *WISE* W1-band and stellar mass TFRs relations of galaxies drawn from the COLD GASS sample, both for an initial sample of all galaxies with available data, and for a restricted sub-sample of galaxies with high-quality measurements

(thus decreasing the scatter). The rotation of the galaxies was determined by fitting the Gaussian Double Peak function to the integrated CO(1-0) line profile of each galaxy, and then measuring the width at 50 per cent of the peak of the resultant fit ( $W_{50}$ ). The W1 magnitudes were drawn directly from the *WISE* catalogue, and the stellar mass for each galaxy was determined via SED fitting of SDSS photometry.

The TFRs obtained from unconstrained forward fits have shallower slopes than those expected from previous studies. Considering only the more robust reverse fits, however, the best-fitting TFRs for the final COLD GASS sub-sample are

$$M_{W1} = (-7.1 \pm 0.6) \left[ \log \left( \frac{W_{50}/\sin i}{\text{km s}^{-1}} \right) - 2.58 \right] - 23.83 \pm 0.09 \quad (13)$$

and

$$\log(M_*/M_{\odot}) = (3.3 \pm 0.3) \left[ \log \left( \frac{W_{50}/\sin i}{\text{km s}^{-1}} \right) - 2.58 \right] + 10.51 \pm 0.04. \quad (14)$$

The unconstrained reverse fit slope of the COLD GASS sub-sample W1-band TFR is still marginally shallower than that of Tully & Pierce (2000), but the slope of the stellar mass TFR agrees within the uncertainties with the relation of Pizagno et al. (2005). The intrinsic scatter (from forward fitting) is  $0.59 \pm 0.05$  mag and  $0.27 \pm 0.02$  dex for the W1-band and stellar mass sub-sample TFR, respectively.

Fixing the slopes to those of the relations from the comparison samples, small offsets are found with respect to the comparison samples, that are, however, less than the intrinsic scatters. The COLD GASS samples therefore agree with the comparison samples, although they have slightly larger scatters than expected. Possible causes of the increased scatters were discussed and include the method adopted to measure inclinations, and fitting a single TFR to samples of galaxies with various primarily late-type morphologies. Importantly, we showed that for a subset of COLD GASS galaxies in the final sub-sample with both CO(1-0) and H I data, the intrinsic and total scatters of the CO(1-0) TFRs were less than those of the same TFRs constructed using H I integrated profiles.

The COLD GASS initial sample and final sub-sample contain a number of galaxies comparable to those in previous CO TFR studies. Our work thus provides a robust local benchmark to be used for comparison with future CO work. In particular, Torii et al. (in preparation) will build a local reference sample based on observations of very nearby galaxies with the NANTEN2 telescope, and utilizing identical fitting methods to ours. Topal et al. (in preparation) will compare the TFRs presented here with those measured using a sample of galaxies at  $z \lesssim 0.3$ , including luminous infrared galaxies and galaxies from the Evolution of Gas in Normal Galaxies survey.

With the dawn of ALMA (and the Northern Extended Millimeter Array<sup>9</sup>), it is now possible to relatively rapidly measure the CO emission of galaxies to large redshifts, when the first objects were forming and slowly settling into the discs we see today. In particular, significant samples of galaxies observed in CO are now being built to probe the epoch of peak global star formation activity ( $1 \lesssim z \lesssim 3$ ), when turbulent gas-rich galaxies were building the bulk of their

<sup>9</sup> <http://iram-institute.org/EN/noema-project.php>

stellar mass. Our work therefore provide a robust reference point with which to compare future TFR studies of those objects.

## ACKNOWLEDGEMENTS

We thank the anonymous referee for their constructive review of this work. AT acknowledges support from an STFC Studentship. MB acknowledges support from STFC rolling grants ‘Astrophysics at Oxford’ ST/H002456/1 and ST/K00106X/1. ST was supported by the Republic of Turkey, Ministry of National Education, and The Philip Wetton Graduate Scholarship at Christ Church. TAD acknowledges support from a Science and Technology Facilities Council Ernest Rutherford Fellowship. We thank the COLD GASS team for kindly providing us with additional data for this work.

This research has made use of the NASA/IPAC Extragalactic Database (NED) which is operated by the Jet Propulsion Laboratory, California Institute of Technology, under contract with the National Aeronautics and Space Administration.

## REFERENCES

- Aaranson M., 1983, *Highlights Astron.*, 6, 269
- Abdalla F. B. et al., 2015, *Proc. Sci., Advancing Astrophysics with the Square Kilometre Array (AASKA14)*. SISSA, Trieste, PoS#17
- Baldwin J. A., Phillips M. M., Terlevich R., 1981, *PASP*, 93, 5
- Bell E. F., de Jong R. S., 2001, *ApJ*, 550, 212
- Bottinelli L., Gougouenheim L., Paturel G., de Vaucouleurs G., 1980, *ApJ*, 242, L153
- Bottinelli L., Gougouenheim L., Teerikorpi P., 1988, *A&A*, 196, 17
- Bruzual G., Charlot S., 2003, *MNRAS*, 344, 1000
- Bureau M., Mould J. R., Staveley-Smith L., 1996, *ApJ*, 463, 60
- Cappellari M., Emsellem E., 2004, *PASP*, 116, 138
- Casertano S. P. R., Shostak G. S., 1980, *A&A*, 81, 371
- Catinella B. et al., 2010, *MNRAS*, 403, 683
- Catinella B. et al., 2012, *A&A*, 544, A65
- Catinella B. et al., 2013, *MNRAS*, 436, 34
- Chabrier G., 2003, *PASP*, 115, 763
- Cole S., Kaiser N., 1989, *MNRAS*, 237, 1127
- Combes F., 2013, in Kawabe R., Kuno N., Yamamoto S., eds, *ASP Conf. Ser. Vol. 476, New Trends in Radio Astronomy in the ALMA Era: The 30th Anniversary of Nobeyama Radio Observatory*. Astron. Soc. Pac., San Francisco, p. 23
- Conselice C. J., Bundy K., Ellis R. S., Brichmann J., Vogt N. P., Phillips A. C., 2005, *ApJ*, 628, 160
- Cresci G. et al., 2009, *ApJ*, 697, 115
- Crocker A. et al., 2012, *MNRAS*, 421, 1298
- Daddi E. et al., 2010, *ApJ*, 714, L118
- Davis T. A. et al., 2011, *MNRAS*, 414, 968
- Davis T. A. et al., 2013, *MNRAS*, 429, 534
- Davis T. A., Greene J., Ma C.-P., Pandya V., Blakeslee J. P., McConnell N., Thomas J., 2016, *MNRAS*, 455, 214
- de Blok W. J. G., 2011, in Carignan C., Combes F., Freeman K. C., eds, *Proc. IAU Symp. 277, Tracing the Ancestry of Galaxies: On the Land of our Ancestors*. Kluwer, Dordrecht, p. 96
- den Heijer M. et al., 2015, *A&A*, 581, A98
- Dickinson M., Papovich C., Ferguson H. C., Budavári T., 2003, *ApJ*, 587, 25
- Duffy A. R., Meyer M. J., Staveley-Smith L., Bernyk M., Croton D. J., Koribalski B. S., Gerstmann D., Westerlund S., 2012, *MNRAS*, 426, 3385
- Eisenstein D. J., Loeb A., 1996, *ApJ*, 459, 432
- Ekholm T., Lanoix P., Teerikorpi P., Fouqué P., Paturel G., 2000, *A&A*, 355, 835
- Förster Schreiber N. M. et al., 2006, *ApJ*, 645, 1062
- Fouque P., Bottinelli L., Gougouenheim L., Paturel G., 1990, *ApJ*, 349, 1
- Freundlich J. et al., 2013, *A&A*, 553, A130
- Genzel R. et al., 2015, *ApJ*, 800, 20
- Giovanelli R., Haynes M. P., da Costa L. N., Freudling W., Salzer J. J., Wegner G., 1997, *ApJ*, 477, L1
- Giovanelli R. et al., 2005, *AJ*, 130, 2598
- Gnedin O. Y., Weinberg D. H., Pizagno J., Prada F., Rix H.-W., 2007, *ApJ*, 671, 1115
- Gnerucci A. et al., 2011, *A&A*, 528, A88
- Haynes M. P. et al., 2011, *AJ*, 142, 170
- Holwerda B., Blyth S., 2010, *ISKAF2010 Science Meeting*. p. 68
- Kauffmann G. et al., 2003, *MNRAS*, 346, 1055
- Kewley L. J., Dopita M. A., Sutherland R. S., Heisler C. A., Trevena J., 2001, *ApJ*, 556, 121
- Kroupa P., 2001, *MNRAS*, 322, 231
- Lagattuta D. J., Mould J. R., Staveley-Smith L., Hong T., Springob C. M., Masters K. L., Koribalski B. S., Jones D. H., 2013, *ApJ*, 771, 88
- Lavezzi T. E., Dickey J. M., 1997, *AJ*, 114, 2437
- Lavezzi T. E., Dickey J. M., 1998, *AJ*, 116, 2672
- Lawrence A. et al., 2007, *MNRAS*, 379, 1599
- Lintott C. J. et al., 2008, *MNRAS*, 389, 1179
- Lintott C. et al., 2011, *MNRAS*, 410, 166
- McGaugh S. S., 2012, *AJ*, 143, 40
- McGaugh S. S., de Blok W. J. G., 1998, *ApJ*, 499, 41
- Madau P., Dickinson M., 2014, *ARA&A*, 52, 415
- Magdis G. E. et al., 2012, *ApJ*, 758, L9
- Magnelli B. et al., 2012, *A&A*, 548, A22
- Maloney P., Black J. H., 1988, *ApJ*, 325, 389
- Markwardt C. B., 2009, in Bohlender D. A., Durand D., Dowler P., eds, *ASP Conf. Ser. Vol. 411, Astronomical Data Analysis Software and Systems XVIII*. Astron. Soc. Pac., San Francisco, p. 251
- Martin D. C. et al., 2005, *ApJ*, 619, L1
- Masters K. L., Springob C. M., Huchra J. P., 2008, *AJ*, 135, 1738
- Meyer M., 2009, in Heald G., Serra P., eds, *Proc. Sci., Panoramic Radio Astronomy: Wide-field 1-2 GHz Research on Galaxy Evolution*. SISSA, Trieste, PoS#15
- Miller S. H., Bundy K., Sullivan M., Ellis R. S., Treu T., 2011, *ApJ*, 741, 115
- Miller S. H., Ellis R. S., Sullivan M., Bundy K., Newman A. B., Treu T., 2012, *ApJ*, 753, 74
- Morganti R. et al., 2006, *MNRAS*, 371, 157
- Morrissey P. et al., 2005, *ApJ*, 619, L7
- Obreschkow D., Croton D., De Lucia G., Khochfar S., Rawlings S., 2009a, *ApJ*, 698, 1467
- Obreschkow D., Klöckner H.-R., Heywood I., Levrier F., Rawlings S., 2009b, *ApJ*, 703, 1890
- Pizagno J. et al., 2005, *ApJ*, 633, 844
- Pizagno J. et al., 2007, *AJ*, 134, 945
- Puech M. et al., 2008, *A&A*, 484, 173
- Riechers D. A., Walter F., Carilli C. L., Bertoldi F., Momjian E., 2008a, *ApJ*, 686, L9
- Riechers D. A., Walter F., Brewer B. J., Carilli C. L., Lewis G. F., Bertoldi F., Cox P., 2008b, *ApJ*, 686, 851
- Riechers D. A. et al., 2009, *ApJ*, 703, 1338
- Saintonge A., 2007, *AJ*, 133, 2087
- Saintonge A. et al., 2011, *MNRAS*, 415, 32
- Sakai S. et al., 2000, *ApJ*, 529, 698
- Salim S. et al., 2007, *ApJS*, 173, 267
- Sandage A., 1988, *ApJ*, 331, 583
- Sandage A., Tammann G. A., 1976, *ApJ*, 210, 7
- Sarzi M. et al., 2006, *MNRAS*, 366, 1151
- Schawinski K., Thomas D., Sarzi M., Maraston C., Kaviraj S., Joo S.-J., Yi S. K., Silk J., 2007, *MNRAS*, 382, 1415
- Schechter P. L., 1980, *AJ*, 85, 801
- Schlafly E. F., Finkbeiner D. P., 2011, *ApJ*, 737, 103
- Serra P. et al., 2012, *MNRAS*, 422, 1835
- Skrutskie M. F. et al., 2006, *AJ*, 131, 1163
- Sorce J. G. et al., 2013, *ApJ*, 765, 94
- Sprayberry D., Bernstein G. M., Impey C. D., Bothun G. D., 1995, *ApJ*, 438, 72

- Steinmetz M., Navarro J. F., 1999, ApJ, 513, 555  
 Stott J. P. et al., 2016, MNRAS, 457, 1888  
 Swinbank A. M., Smail I., Sobral D., Theuns T., Best P. N., Geach J. E., 2012, ApJ, 760, 130  
 Tacconi L. J. et al., 2010, Nature, 463, 781  
 Tacconi L. J. et al., 2013, ApJ, 768, 74  
 Teerikorpi P., 1987, A&A, 173, 39  
 Theureau G., Hanski M. O., Coudreau N., Hallet N., Martin J.-M., 2007, A&A, 465, 71  
 Tiley A. L. et al., 2016, MNRAS, 460, 103  
 Tully R. B., Courtois H. M., 2012, ApJ, 749, 78  
 Tully R. B., Fisher J. R., 1977, A&A, 54, 661  
 Tully R. B., Pierce M. J., 2000, ApJ, 533, 744  
 Tutui Y., Sofue Y., Honma M., Ichikawa T., Wakamatsu K.-I., 2001, PASJ, 53, 701  
 van den Bosch F. C., 2000, ApJ, 530, 177  
 Verheijen M. A. W., 2001, ApJ, 563, 694  
 Wagg J. et al., 2014, ApJ, 783, 71  
 Walter F., Carilli C., Bertoldi F., Menten K., Cox P., Lo K. Y., Fan X., Strauss M. A., 2004, ApJ, 615, L17  
 Wang R. et al., 2011, AJ, 142, 101  
 Westmeier T., Jurek R., Obreschkow D., Koribalski B. S., Staveley-Smith L., 2014, MNRAS, 438, 1176  
 Wiklind T., Combes F., Henkel C., Wyrowski F., 1997, A&A, 323, 727  
 Williams M. J., Bureau M., Cappellari M., 2010, MNRAS, 409, 1330  
 Willick J. A., 1994, ApJS, 92, 1  
 Willick J. A., Courteau S., Faber S. M., Burstein D., Dekel A., 1995, ApJ, 446, 12  
 Willick J. A., Strauss M. A., Dekel A., Kolatt T., 1997, ApJ, 486, 629  
 Wisnioski E. et al., 2015, ApJ, 799, 209  
 Wright E. L. et al., 2010, AJ, 140, 1868  
 Yahya S., Bull P., Santos M. G., Silva M., Maartens R., Okouma P., Bassett B., 2015, MNRAS, 450, 2251  
 Yang X., Mo H. J., van den Bosch F. C., 2003, MNRAS, 339, 1057  
 York D. G. et al., 2000, AJ, 120, 1579  
 Yuan H. B., Liu X. W., Xiang M. S., 2013, MNRAS, 430, 2188  
 Ziegler B. L. et al., 2002, ApJ, 564, L69

## APPENDIX A: VELOCITY MEASURE: $W_{50}$

### A1 Fitting functions

As stated in Section 3.1, as a characteristic velocity measure, we adopt  $W_{50}$ , the width of the CO(1–0) integrated profile at 50 per cent of its maximum. Given the non-negligible noise in the COLD GASS spectra, a fit to the profile is preferred to a direct measurement of  $W_{50}$ . However, the choice of the fitting function is not trivial and several different functions have been used in the past. In this section, we examine the relative merits of several of these functions for measuring  $W_{50}$ . Our goal is to ascertain which function is the most accurate and most importantly minimizes potential biases as a function of  $A/N$ , inclination (apparent width) and rotation velocity (intrinsic width) (all related to the total  $S/N$ ).

The functions compared include the standard single Gaussian,

$$f(v) = A e^{-\frac{(v-v_0)^2}{2\sigma^2}}, \quad (\text{A1})$$

where  $v$  is the velocity,  $A > 0$  is the amplitude of the peak (maximum flux),  $v_0$  is the velocity of the peak (and mean velocity); taken to be within  $\pm 500 \text{ km s}^{-1}$  of the known systemic velocity), and  $\sigma > 11.5 \text{ km s}^{-1}$  (the velocity bin width of the COLD GASS spectra) is the rms velocity (i.e. the velocity width) of the profile.

We also test a symmetric (with respect to the central velocity) Gaussian Double Peak function, composed of a parabolic function surrounded by two equidistant and identical (but mirrored) half-

Gaussians forming the low- and high-velocity edges of the profile:

$$f(v) = \begin{cases} A_G \times e^{-\frac{-(v-(v_0-w))^2}{2\sigma^2}} & v < v_0 - w \\ A_C + a(v - v_0)^2 & v_0 - w \leq v \leq v_0 + w, \\ A_G \times e^{-\frac{-(v-(v_0+w))^2}{2\sigma^2}} & v > v_0 + w \end{cases} \quad (\text{A2})$$

where  $v_0$  is the central (mean) velocity (again taken to be within  $\pm 500 \text{ km s}^{-1}$  of the known systemic velocity),  $w > 0$  is the half-width of the central parabola,  $\sigma > 0 \text{ km s}^{-1}$  is the width of the profile edges,  $A_G > 0$  is the peak flux of the two half-Gaussians (centred at  $v_0 \pm w$ ),  $A_C > 0$  is the flux at the central velocity, and  $a = (A_G - A_C) / w^2$ .

A variation of the Gaussian Double Peak function was also tested, the Exponential Double Peak function used by Crocker et al. (2012), where the two half-Gaussian edges are replaced by exponentials:

$$f(v) = \begin{cases} A_G \times e^{-\frac{|v-(v_0-w)|}{\sigma}} & v < v_0 - w \\ A_C + a(v - v_0)^2 & v_0 - w \leq v \leq v_0 + w, \\ A_G \times e^{-\frac{|v-(v_0+w)|}{\sigma}} & v > v_0 + w \end{cases} \quad (\text{A3})$$

where  $A_G > 0$  is the peak flux of the two exponentials, but all the parameters otherwise have the same meaning as for the Gaussian Double Peak function.

Finally, a fourth function was also tested, the generalized Busy Function adopted and discussed in detail by Westmeier et al. (2014). Briefly, it is the product of two error functions,  $\text{erf}(x)$  and a polynomial. The resulting shape is similar to that of the double-peaked functions above, i.e. typically a peak (from the error functions) on either side of a central dip (from the polynomial). The generalized form is described by

$$B(v) = \frac{a}{4} \times \{\text{erf}[b_1(v - \gamma_1)] + 1\} \\ \times \{\text{erf}[b_2(\gamma_2 - v)] + 1\} \\ \times (c|v - v_p|^n + 1), \quad (\text{A4})$$

where  $b_1 > 0$  and  $b_2 > 0$  are, respectively, the slope of the left and right error function, whilst  $\gamma_1$  and  $\gamma_2$  describe their respective width.  $n, c > 0$  and  $v_p$  are, respectively, the order, slope and offset of the polynomial. We adopted  $n = 2$ , yielding a parabola as for the double-peaked functions above.  $a > 0$  determines the normalization of the profile.

### A2 Tests

To test which fitting function is most appropriate, a library of noiseless integrated spectra was generated using the KINematic Molecular Simulation (KINMS<sup>10</sup>) routine of Davis et al. (2013). Since the overall  $S/N$  is a function of both  $A/N$  and the profile width, while we are ultimately only interested in recovering the profile width for TFR studies, we have decided to probe the effects of these two parameters separately.

The shape of a galaxy's integrated CO emission profile is primarily dependent on the physical properties of the galaxy, and to a lesser extent on the nature of the telescope used to observe it. Broadly, the width of the profile depends on the galaxy's projected circular velocity, and therefore its dynamical mass (Casertano & Shostak 1980), whilst the breadth of the flanks of the profile depends on

<sup>10</sup> [purl.org/KinMS](http://purl.org/KinMS)

the intrinsic turbulence of the gas. The integral of the profile is proportional to the galaxy's total molecular gas mass (e.g. Maloney & Black 1988). The overall shape of the profile also depends on the distribution of the gas within the galaxy: the radial density profile will determine to what extent the CO emission samples the flat part of the galaxy's rotation curve – if the gas extends out to sufficient radii, the intrinsic profile will display a double-horned or boxy shape (e.g. Davis et al. 2011). Additionally, the central flux of the profile (and thus whether it is intrinsically double-horned or boxy) depends on the gas concentration within the disc (e.g. Wiklind et al. 1997; Lavezzi & Dickey 1997, see Section 3.3). Whether or not the observed profile appears Gaussian, boxy or double-horned also depends on the width of the velocity channels and the beam size of the telescope used to observe the galaxy; if the velocity channels are too broad or the beam size is smaller than the radial size of the galaxy, then the integrated emission profile may appear Gaussian despite being intrinsically boxy or double-horned (in the latter case, it is not a true integrated profile).

Bearing all this in mind, the model spectra were created by assuming an edge-on exponential disc of molecular gas with a scalelength of 2 arcsec, a realistic circular velocity curve that peaks at 3 arcsec and then remains flat, and a fixed molecular gas velocity dispersion of 12 km s<sup>-1</sup>. A Gaussian single-dish telescope response with a 22 arcsec beam (full width at half-maximum) was used to integrate the flux spatially, matching that of the IRAM 30 m telescope. This also ensures that our spectra contain essentially all the flux of the modelled discs, and the resulting spectra are intrinsically double-horned or boxy-shaped.

Model-integrated spectra with flat circular velocities  $V_{c, \text{flat}}$  ranging from 70 to 385 km s<sup>-1</sup>, and with inclinations ranging from 5° to 85°, were generated and then binned to 11.5 km s<sup>-1</sup> per channel to match the COLD GASS spectra. Each of the resulting spectra was then degraded by adding random Gaussian noise such that the desired  $A/N$  was reached, where the amplitude  $A$  is defined here as the peak of the spectrum before noise was added, and the noise  $N$  is defined as the rms of the spectrum in an area devoid of emission (thus equal to the dispersion of the Gaussian used to generate the noise).

For each input circular velocity  $V_{c, \text{flat}}$ , inclination  $i$  and amplitude-to-noise ratio  $A/N$ , 150 realizations of the resulting model spectrum were generated. Each of these realizations was then fit with the four different functions described in Section A1, and the width of the best-fitting profile at 50 per cent of the peak ( $W_{50}$ ) was calculated. The fits were carried out using the PYTHON package MPFIT<sup>11</sup> (Markwardt 2009; translated into PYTHON by Mark River and updated by Sergey Koposov), that employs a Levenberg–Marquardt minimization algorithm. The adopted  $W_{50}$  and its uncertainty for each combination of  $V_{c, \text{flat}}$ ,  $i$  and  $A/N$  were then taken, respectively, as the median and median absolute deviation (with respect to the median itself) of the 150 associated measurements.

Fig. A1 shows the fractional difference between the true width ( $W_{50, \text{true}}$ ), defined as  $W_{50}$  measured at  $A/N = 10000$  (i.e. for an effectively noiseless spectrum), and that measured as a function of  $A/N$ , this for the case where  $V_{c, \text{flat}} = 210$  km s<sup>-1</sup>, and  $i = 70^\circ$ . We do not show the results for every combination of velocity and inclination that we tested, but rather select this case as an illustrative example. We do, however, summarize the results for each function tested in the four panels of Fig. A2. This shows how self-consistent each of the four tested functions is as a function of  $V_{c, \text{flat}}$  and  $i$ , where self-consistency is taken here to mean both that the measured width

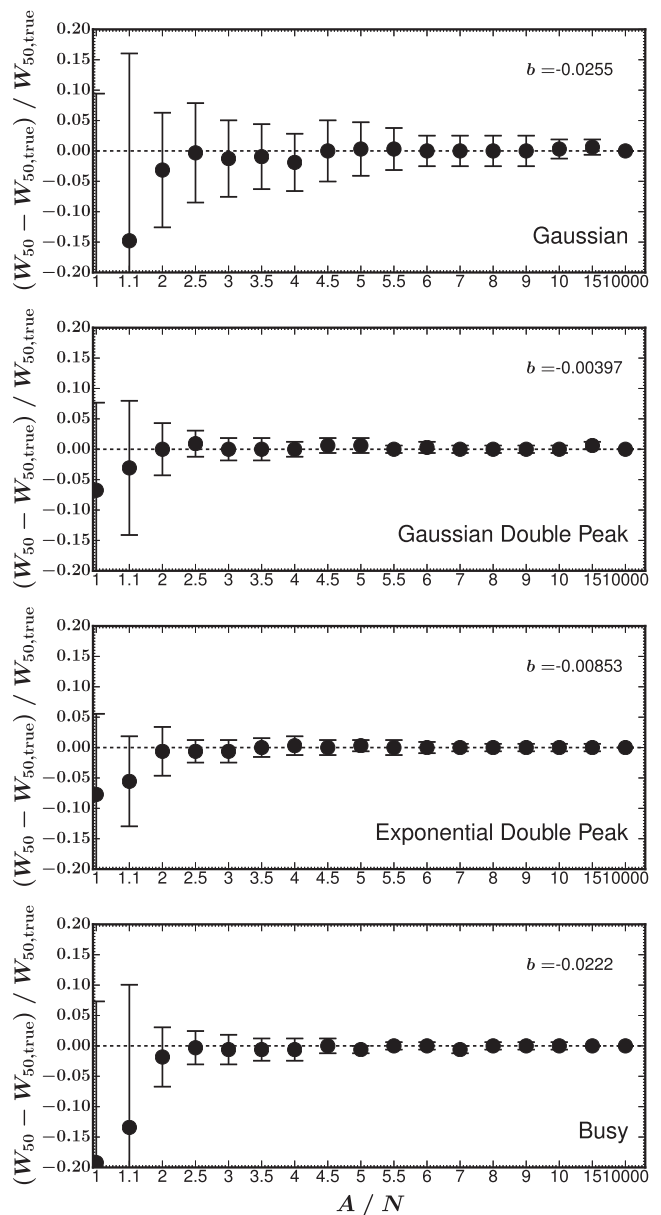


**Figure A1.** Fractional difference between  $W_{50}$  measured at  $A/N = 10000$  ( $W_{50, \text{true}}$ , effectively noiseless) and  $W_{50}$  measured for various values of  $A/N$ , this for an example case where the velocity  $V_{c, \text{flat}} = 210$  km s<sup>-1</sup> and inclination  $i = 70^\circ$ . The four panels show how consistent the measured  $W_{50}$  is for each of the four functions discussed in Section A1 (i.e. Gaussian, Gaussian Double Peak, Exponential Double Peak, and Busy function). We quantify this with a bias measure  $b$  defined in Section A2 and shown in the top-right corner of each panel.

is similar to its true value and that it does not vary systematically with decreasing  $A/N$ . This is judged by measuring the bias  $b$ , defined as the average fractional width difference over all  $A/N$  sampled. The bias for each function, and for each of the selected values of  $V_{c, \text{flat}}$  and  $i$ , is shown in the panels of Fig. A2. It is clear that both Double Peak functions overestimate to varying degrees the linewidth (with respect to  $W_{50, \text{true}}$ ) for low values of inclination ( $i \lesssim 20^\circ$ ), but are otherwise only slightly negatively biased. The Busy function displays the same trends, but is negatively biased to a greater degree than the Double Peak functions for high values of inclination ( $i \gtrsim 20^\circ$ ). The Gaussian function, however, is negatively

<sup>11</sup> <https://code.google.com/p/astrolibpy/source/browse/mpfit/mpfit.py>

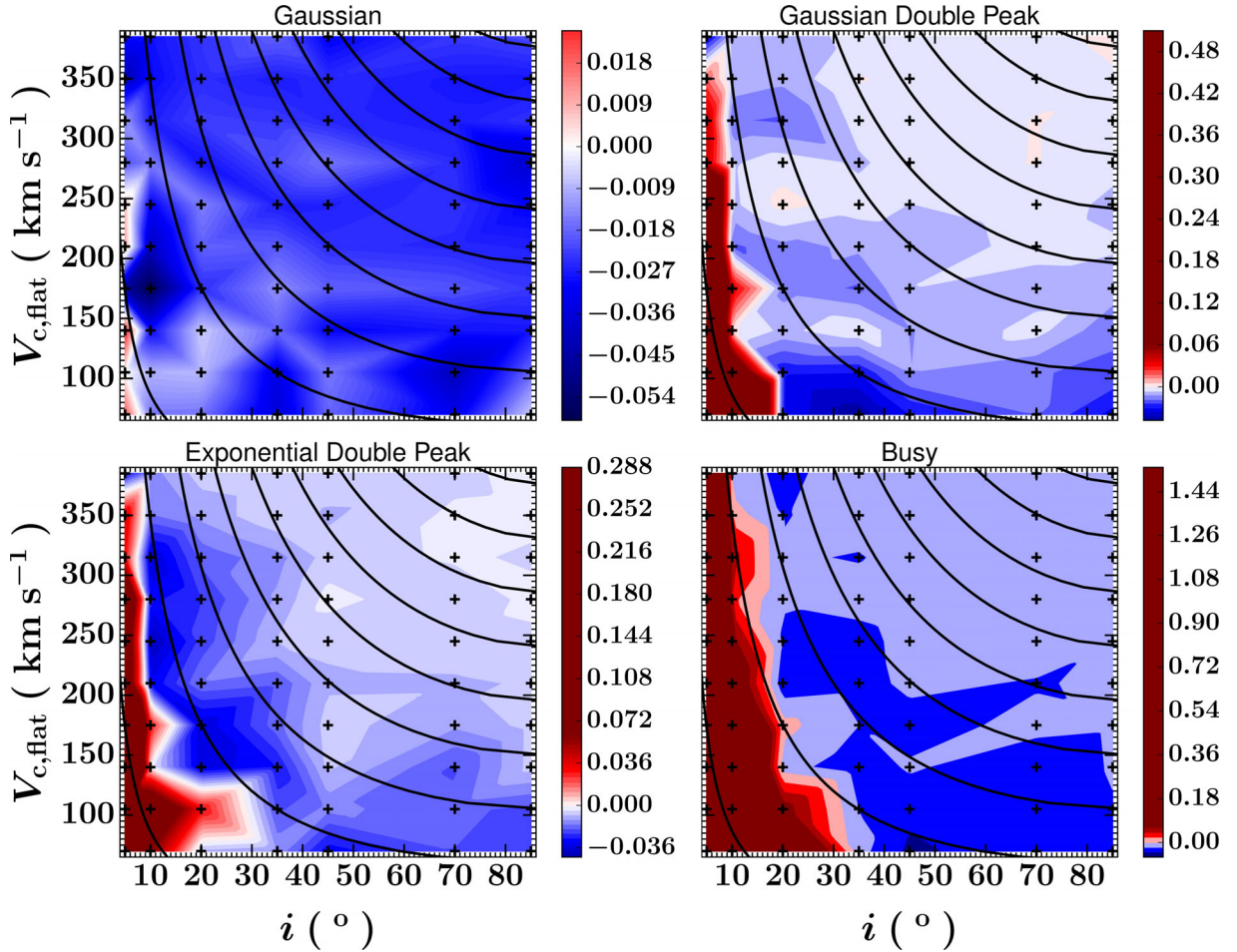
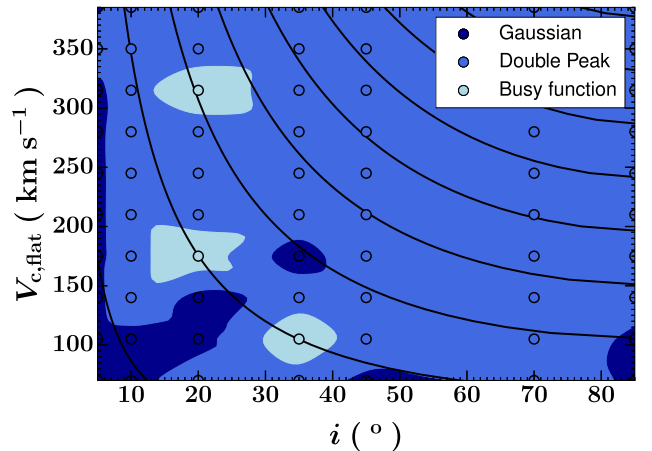


**Figure A2.** The bias  $b$  (as defined in the text) of the four analytical functions considered, as a function of the circular velocity  $V_{c, \text{flat}}$  and the inclination  $i$ . For each function, the common colour scale shows whether the fit is positively (red) or negatively (blue) biased. The data points (black crosses) indicate  $V_{c, \text{flat}}-i$  pairs where a measurement was made. Black lines show curves of constant  $V_{c, \text{flat}} \sin i$ .

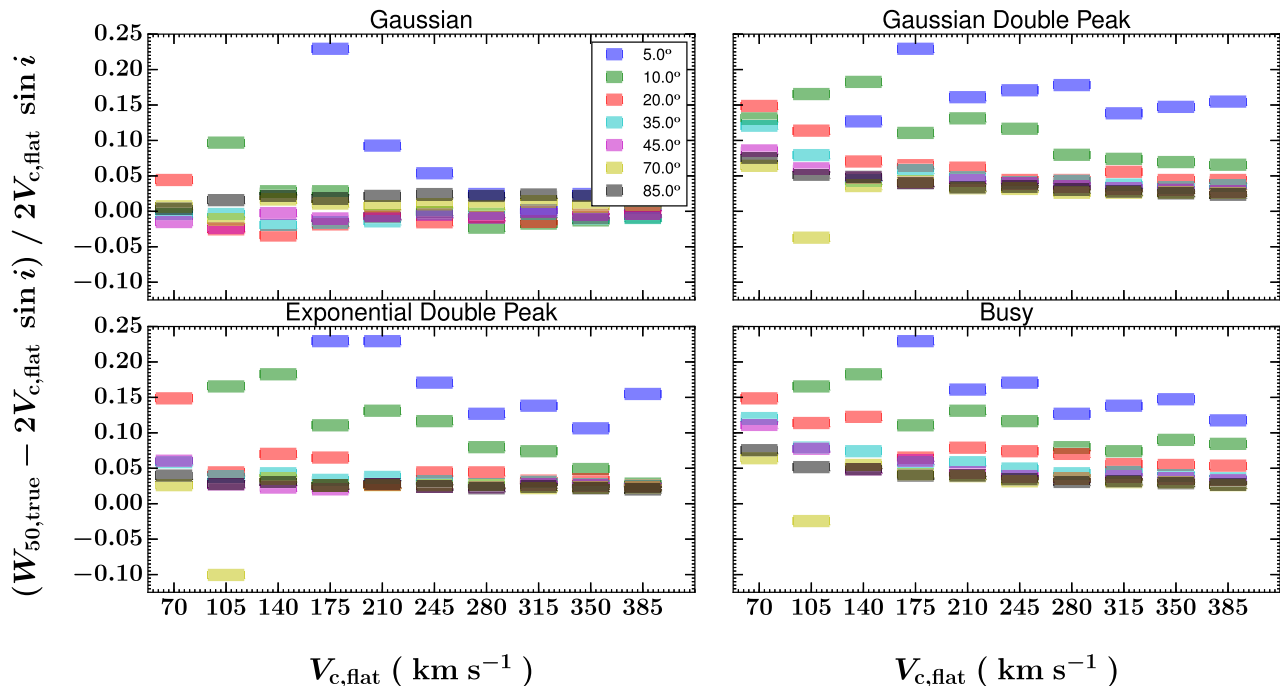
biased in most cases, and to a greater degree than each of the three other functions.

Fig. A3 attempts to distill further the information contained in Fig. A2. It shows which function is most self-consistent as a function of  $V_{c, \text{flat}}$  and  $i$ , where self-consistency is again judged by the bias  $b$ . We found that the Gaussian Double Peak and Exponential Double Peak functions yield very similar results in terms of self-consistency, recovering the true width to a similar accuracy at a given circular velocity, inclination and amplitude-to-noise ratio. This is clear in the panels of Fig. A2. Given the restricted velocity resolution of the COLD GASS spectra, and since the only real difference between the Gaussian Double Peak and the Exponential Double Peak function is the shape of the edges, it was decided to group these two functions together when considering their self-consistency with respect to that of the Gaussian and Busy functions.

What is immediately obvious from Fig. A3 is that the Busy function features very little in the plot; it was rarely the most self-consistent function. The main result is that the double-peaked functions are the most self-consistent in the majority of cases, be it the Gaussian Double Peak or the Exponential Double Peak function. The single Gaussian is the most self-consistent only at small inclinations (i.e. face-on discs) or small circular velocities. These two extremes are of course degenerate observationally, and this result is easily understood. Indeed, since any galaxy spectrum has a finite spectral resolution, the integrated velocity profile will appear



**Figure A3.** Self-consistency (as defined in the text) of the four analytical functions considered, as a function of the circular velocity  $V_{c, \text{flat}}$  and the inclination  $i$ . The colour coding shows which function is most self-consistent (dark blue: Gaussian function; blue: either of the Gaussian Double Peak or Exponential Double Peak function; light blue: Busy function). The data points (open circles) indicate  $V_{c, \text{flat}}-i$  pairs where a measurement was made. The underlying colour scale shows tri-tonal contours of the same measurements, for ease of interpretation. Black lines show curves of constant  $V_{c, \text{flat}} \sin i$ . The Double Peak functions are the most self-consistent in the majority of the cases tested.



**Figure A4.** Fractional difference between the true width recovered ( $W_{50,\text{true}}$ ,  $W_{50}$  for  $A/N = 10\,000$ ) and twice the projected input circular velocity  $2V_{c,\text{flat}} \sin i$ , this as a function of  $V_{c,\text{flat}}$  itself for different inclinations  $i$ . Each panel shows a different fitting function. In general, measurements of  $W_{50,\text{true}}$  are reasonably constant (as a function of  $V_{c,\text{flat}}$ ) for  $i \geq 35^\circ$  only.

Gaussian regardless of its intrinsic shape if the inclination or the circular velocity is small enough.

In addition to self-consistency, one should also consider how accurately each function recovers the circular velocity. For each of the four functions tested, Fig. A4 thus shows the fractional difference between the true width ( $W_{50,\text{true}}$ ) and (twice) the projected circular velocity  $2V_{c,\text{flat}} \sin i$ , this as a function of  $V_{c,\text{flat}}$  itself and for different values of the inclination  $i$ . In other words, Fig. A4 summarizes the position of the dashed black line, with respect to  $2V_{c,\text{flat}} \sin i$ , in each of the panels of Fig. A1 (but now for every velocity and inclination tested).

We recall here that a constant fractional offset is unimportant for TFR work, but that useful functions will minimize any systematic variation with circular velocity (and  $A/N$ ). Fig. A4 thus clearly shows that no function yields constant  $W_{50,\text{true}}$  measurements (as a function of  $V_{c,\text{flat}}$ ) at inclinations  $i \leq 10^\circ$ , only the Gaussian Double Peak function does a reasonable job at  $i = 20^\circ$ , and all functions are satisfactory at  $i \geq 35^\circ$ .

Given that the cases in which the Gaussian function is most self-consistent cover only a small area in the parameter space of  $V_{c,\text{flat}}$  and  $i$  (see Fig. A3), and given that no function yields constant measurements at small  $i$  (Fig. A4), two conclusions must be drawn. First, galaxies observed at small inclinations ( $i \leq 30^\circ$ ) should be avoided. Secondly, the Gaussian Double Peak function is the most appropriate function with which to measure the CO(1–0) linewidths of the COLD GASS galaxies (the Gaussian form of the profile’s edge is also better justified physically than the exponential form). It should, however, be stressed that these conclusions are drawn here exclusively from simulated spectra with an intrinsic regular double-horned shape.

## APPENDIX B: COMPARISON WITH H I

In Section 1.2, we discussed the relative advantages of constructing the TFR using CO(1–0) as a dynamical tracer rather than H I, the

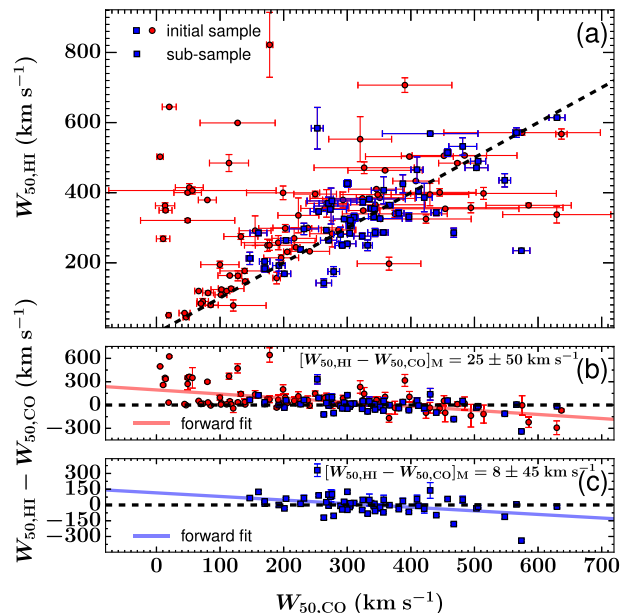


**Figure B1.** Comparison between  $W_{50,\text{CO}}$  and  $W_{50,\text{H1}}$  for galaxies in the initial sample (see Section 2; red circles and blue squares), and the final sub-sample (see Section 3.3; blue squares) that have a corresponding H I detection in GASS. (a) Correlation between the two measures of linewidth for both the initial sample and sub-sample. The dashed black line represents the 1:1 relation. (b) and (c) line-width difference  $W_{50,\text{H1}} - W_{50,\text{CO}}$  for the initial sample and sub-sample, respectively. The red solid line ( $W_{50,\text{H1}} - W_{50,\text{CO}} = (-0.53 \pm 0.07)[W_{50,\text{CO}} - 277.4] + 48 \pm 10$ ) and blue solid line ( $W_{50,\text{H1}} - W_{50,\text{CO}} = (-0.3 \pm 0.1)[W_{50,\text{CO}} - 323.5] + 5 \pm 11$ ) represent a free forward fit to the data points in, respectively, (b) and (c). The median difference is displayed in the top right of both (b) and (c), along with its uncertainty (the median absolute deviation from the median itself).  $W_{50,\text{CO}}$  and  $W_{50,\text{H1}}$  differ much less for galaxies in the final sub-sample than for galaxies only included in the initial sample.

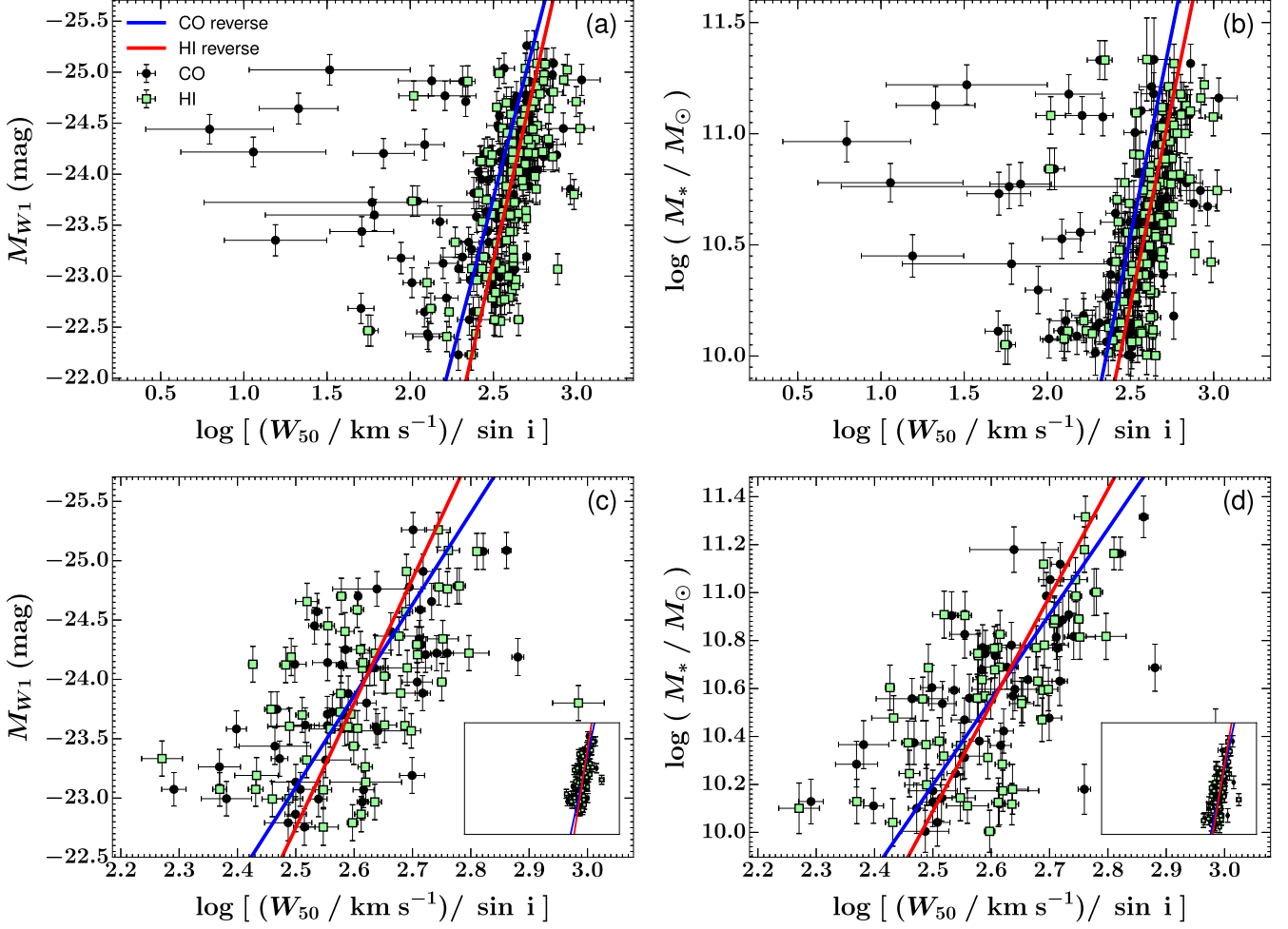


**Figure B2.** Comparison of the  $W1$ -band and stellar mass Tully–Fisher relations using  $W_{50}$  values derived from COLD GASS CO(1–0) integrated profiles ( $W_{50,\text{CO}}$ , black points) and GASS H I integrated profiles ( $W_{50,\text{H I}}$ , pale green points), this for the same galaxies with both CO and H I data. (a) and (c) show the absolute  $W1$ -band TFR of those galaxies from, respectively, the initial COLD GASS sample and our final sub-sample. The  $x$ -axis is the width of the integrated profile (CO(1–0) or H I) at 50 per cent of the peak, corrected for the effect of inclination. For (a) and (c), the  $y$ -axis is the absolute  $WISE$  Band 1 magnitude  $W1$  ( $\approx 3.4 \mu\text{m}$ ). The solid blue line show the reverse fit to the CO(1–0) data points. The reverse fit to the H I data points is shown as the solid red line. To demonstrate the reduction in scatter between the initial sample and final sub-sample, the embedded panel in (c) shows the TFR for the final sub-sample but over the same axis ranges as (a). (b) and (d) are as (a) and (c), but for the stellar mass TFRs.

**Table B1.** Reverse fit parameters of the  $W1$ -band and stellar mass Tully–Fisher relations presented in Fig. B2. The pivot value is 2.6 for all relations (see Section 3.2).

TFR	Tracer	Sample	Slope	Intercept (dex)	Intrinsic scatter (dex)	Total scatter (dex)
$M_*$	CO	Initial	$4 \pm 2$	$10.9 \pm 0.2$	$0.93 \pm 0.09$	$0.985 \pm 0.007$
		Sub-sample	$3.6 \pm 0.6$	$10.55 \pm 0.04$	$0.28 \pm 0.03$	$0.310 \pm 0.007$
	H I	Initial	$3.6 \pm 0.6$	$10.60 \pm 0.05$	$0.56 \pm 0.04$	$0.580 \pm 0.005$
		Sub-sample	$4.5 \pm 0.9$	$10.53 \pm 0.06$	$0.43 \pm 0.05$	$0.445 \pm 0.009$
$M_{W1}$	CO	Initial	$-6 \pm 1$	$-24.4 \pm 0.2$	$1.6 \pm 0.1$	$1.61 \pm 0.01$
		Sub-sample	$-8 \pm 1$	$-23.9 \pm 0.1$	$0.68 \pm 0.07$	$0.69 \pm 0.01$
	H I	Initial	$-7 \pm 1$	$-23.9 \pm 0.1$	$1.07 \pm 0.07$	$1.104 \pm 0.009$
		Sub-sample	$-10 \pm 3$	$-23.8 \pm 0.2$	$1.1 \pm 0.1$	$1.09 \pm 0.02$

use of the latter being well established. In this section, we compare the values of  $W_{50}$  derived from COLD GASS CO(1–0) integrated profiles to those derived from GASS H I integrated profiles of the same galaxies. We measure the latter by fitting the Double Peak

Gaussian function to the H I spectra in the same manner as described in Section 3.1.

The majority of the GASS H I galaxy spectra were obtained with the Arecibo 305 m telescope (see Section 2.1 for more detail). The



spectra are available as part of the GASS data releases<sup>12</sup> (Catinella et al. 2010, 2012, 2013). However, as described in Catinella et al. (2010), GASS galaxies were not re-observed with Arecibo if a suitable H I detection was already available from the ALFALFA survey or the Cornell H I archive (Haynes et al. 2011). As such, the comparison conducted in this section draws on H I  $W_{50}$  values measured from spectra from all three sources. We denote all measurements of the width of a galaxy’s H I integrated profile at 50 per cent of its maximum as  $W_{50,H\text{I}}$ . For clarity, in this section only, we denote the CO(1–0)  $W_{50}$  values described in Section 3.1 as  $W_{50,\text{CO}}$ .

Of the 207 COLD GASS galaxies in the initial sample defined in Section 2, 155 originate from the COLD GASS DR3, with the remaining 52 from the low-mass extension of COLD GASS. H I spectra for galaxies in the COLD GASS low-mass extension are not publicly available, so we exclude these galaxies from our comparison. Of the remaining 155 galaxies, 140 have a corresponding H I spectrum that is publicly available. We detect a signal (i.e.  $A/N > 1$ ) in 136 of these (76 observed directly by GASS, 38 from ALFALFA and 22 from the Cornell archive). As all 136 of these spectra obey the selection criteria of the initial sample as defined in Section 2, we include them all in our comparison. Of the 83 COLD GASS galaxies comprising the sub-sample defined in Section 3.3, we exclude 17 galaxies that originate from the COLD GASS low-mass extension (for the reason discussed). The remaining 66 galaxies originate from the COLD GASS DR3. 59 of these have a corresponding H I spectrum that is publicly available. To maintain consistency in our comparison, we apply the same selection criteria to the derived H I linewidths as those used to define the sub-sample in Section 3.3. To this end, we exclude two galaxies with  $A/N < 1.5$ , leaving 57 spectra (30 from GASS, 16 from ALFALFA and 11 from the Cornell archive).

We compare the values of  $W_{50,\text{CO}}$  and  $W_{50,H\text{I}}$  for both the initial sample and sub-sample in Fig. B1. This shows that, for both the sample and sub-sample, the two measures of linewidth generally correlate well with one another. However, the scatter around the 1:1 line is much larger for the initial sample than for the sub-sample. The increased scatter in the initial sample is a consequence of the inclusion of galaxies with CO(1–0) integrated profiles that do not display a double-horned or boxy shape, i.e. profiles for which we cannot be sure the CO sufficiently probes the outer parts of the galaxy’s rotation curve (see Section 3.3). Considering only the sub-sample, the two measures of linewidth are in good agreement ( $[W_{50,H\text{I}} - W_{50,\text{CO}}]_{\text{M}} = 8 \pm 45 \text{ km s}^{-1}$ , where the uncertainty is the median absolute deviation with respect to the median itself).

The H I velocity widths are typically larger than the CO velocity widths at lowest values of  $W_{50,\text{CO}}$ , as is apparent from the free fit (solid red) line in panel (b) of Fig. B1. Conversely, for the highest values of  $W_{50,\text{CO}}$ ,  $W_{50,H\text{I}}$  tends to be smaller. This trend is weaker

but still present in the sub-sample, as is shown by the free fit (solid blue) line in panel (c) of Fig. B1.

To investigate whether this bias translates into a significant difference between TFRs constructed using CO(1–0) line-widths and H I linewidths, we plot in Fig. B2 both the W1-band and the stellar mass TFR of both the initial sample and the final sub-sample, this using both  $W_{50,\text{CO}}$  and  $W_{50,H\text{I}}$  values. For consistency, we only consider here galaxies with both CO and H I data. This allows us to directly compare how the use of either measure of linewidth affects the relations. The corresponding TFR fit parameters are listed in Table B1. For reasons discussed in Section 3.4, the reverse fit is preferred to the conventional forward fit (see Section 3.2 for a description of both). In addition, it is more informative here to examine how the scatter in the velocity width changes when considering either  $W_{50,\text{CO}}$  or  $W_{50,H\text{I}}$  than the scatter in the W1 magnitudes or stellar masses. For both these reasons, we examine only the reverse fits to the TFRs, as shown in Fig. B2.

Whilst in all cases the slopes of both the  $W_{50,\text{CO}}$  and  $W_{50,H\text{I}}$  TFRs agree within uncertainties, the slopes of both H I TFRs of the sub-sample are steeper than those of the CO(1–0) TFRs for the same galaxies. The intercepts agree within the uncertainties for all the TFRs of the sub-sample. However, the intercepts of both the stellar mass and W1 CO(1–0) TFRs of the initial sample are offset to higher values along the ordinate compared to those of the corresponding H I relations. For both the stellar mass and W1-band TFRs of the initial sample, the total and intrinsic scatter of the  $W_{50,H\text{I}}$  relations are significantly less than those of the  $W_{50,\text{CO}}$  relations. Conversely, considering the TFRs of the sub-sample, the total and intrinsic scatter of the CO relations are significantly smaller. It is clear then that TFRs constructed using CO and H I linewidths are comparable in terms of slope and intercept, but differ in terms of intrinsic and total scatter. Considering the H I TFRs (both the W1-band and stellar mass relations), there is only a small reduction in the intrinsic and total scatter between the initial sample and the final sub-sample. The reduction in scatter for the CO TFRs is much greater – primarily as a result of excluding from the sub-sample those galaxies with CO(1–0) integrated profiles that do not display a boxy or double-horned shape (see Sections 3.3 and 4.5). We therefore conclude that, assuming the selection criteria of the sub-sample are applied, the CO and H I linewidths, and thus the resultant TFRs, are comparable, but that the scatter is greatly reduced by using CO.

## APPENDIX C: GALAXY SPECTRA

Fig. C1 shows the Gaussian Double Peak function fits to each of the COLD GASS galaxy spectra in our final sub-sample, as described in Sections 3.1 and 3.3. The data are plotted in blue and the best-fitting function in green. The solid red line indicates the best-fitting central velocity ( $v_0$ ), whilst the dashed red lines show the width at 50 per cent of the peak ( $W_{50}$ ).

<sup>12</sup> <http://wwwmpa.mpa-garching.mpg.de/GASS/data.php>

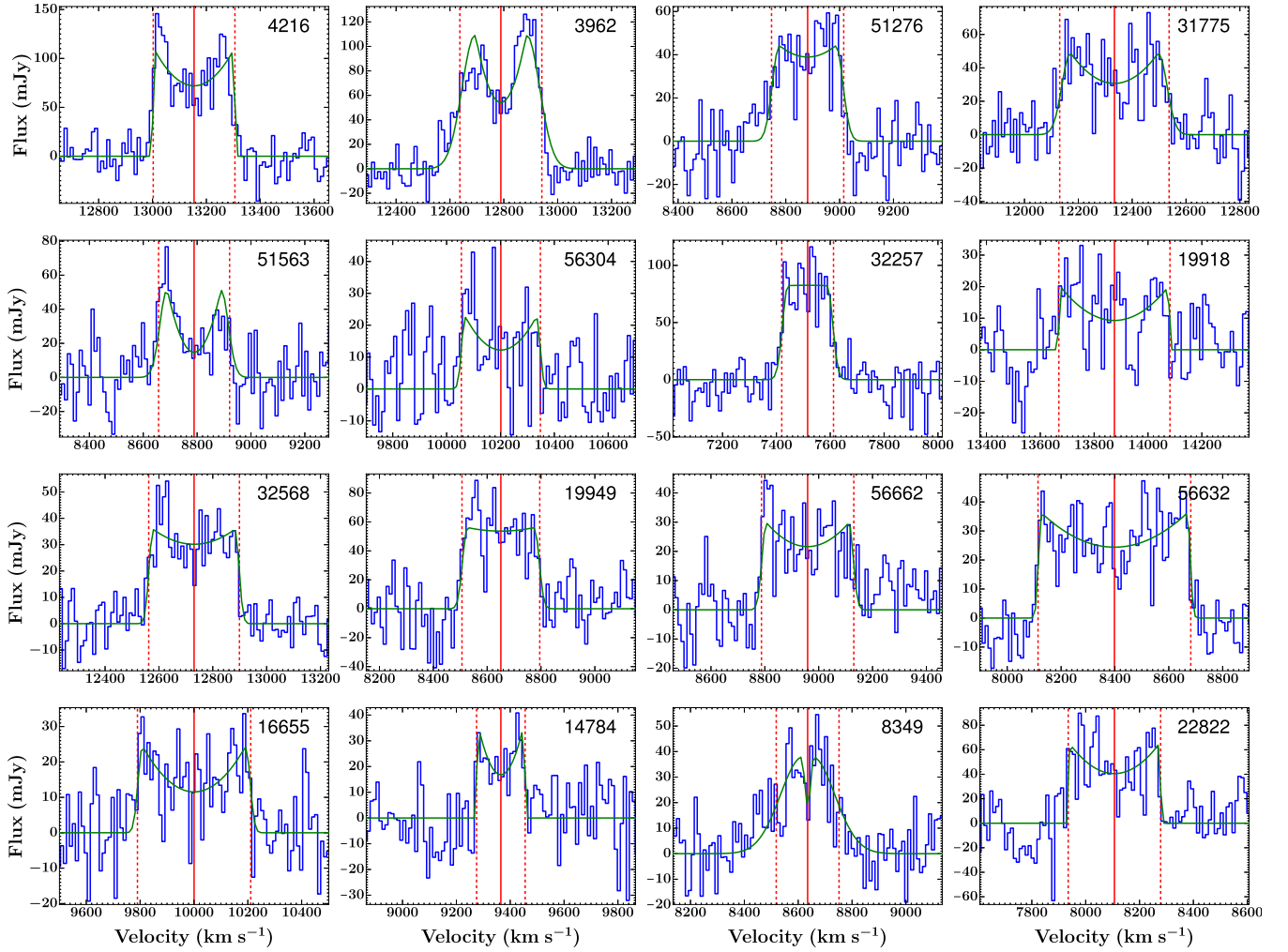


**Figure C1.** The Gaussian Double Peak function fits to each of the COLD GASS galaxy spectra in our final sub-sample, as described in Sections 3.1 and 3.3. The data are plotted in blue and the best-fitting function in green. The solid red line indicates the best-fitting central velocity ( $v_0$ ), whilst the dashed red lines show the width at 50 per cent of the peak ( $W_{50}$ ). The COLD GASS ID is displayed in the top right of each panel.

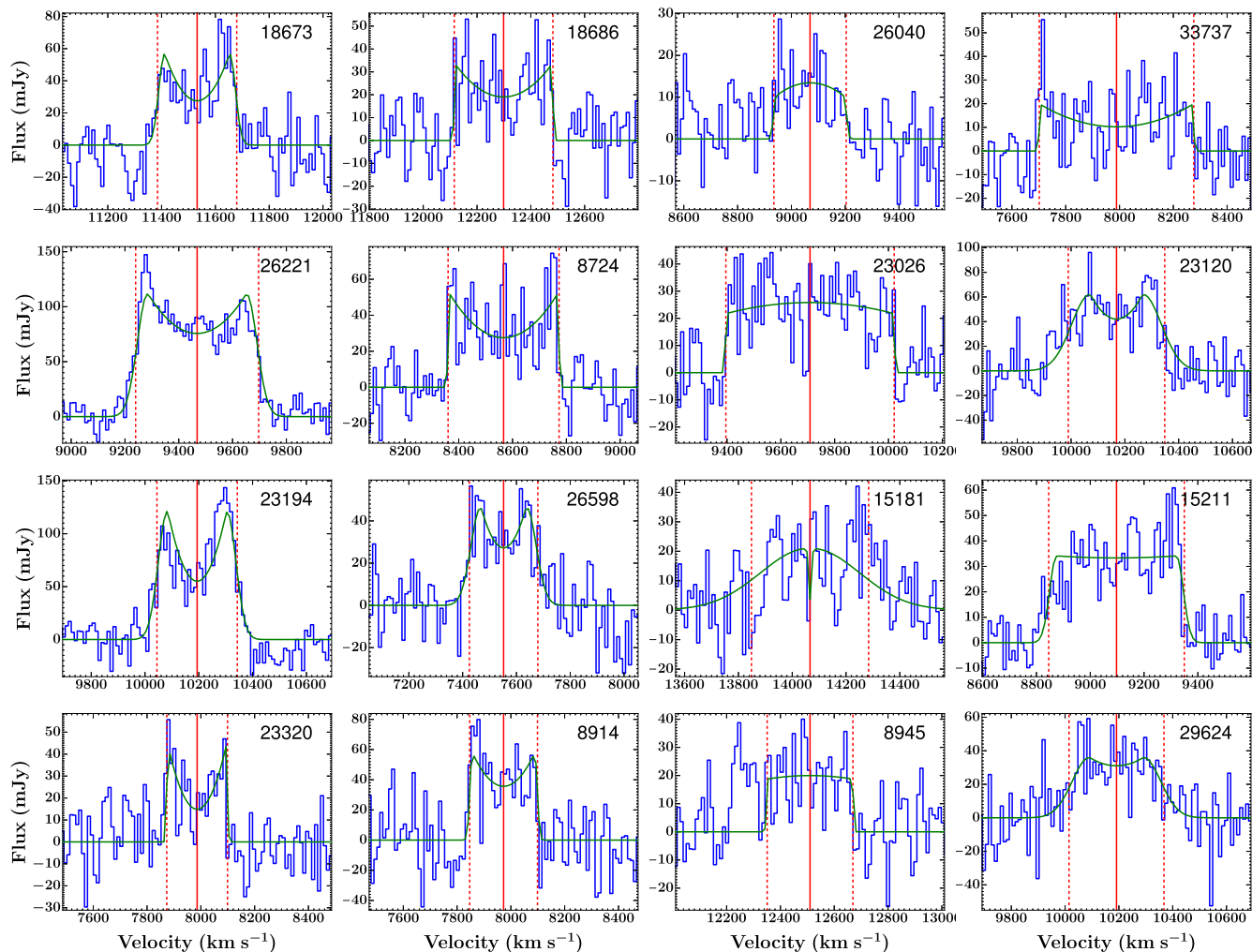


Figure C1 – *continued*

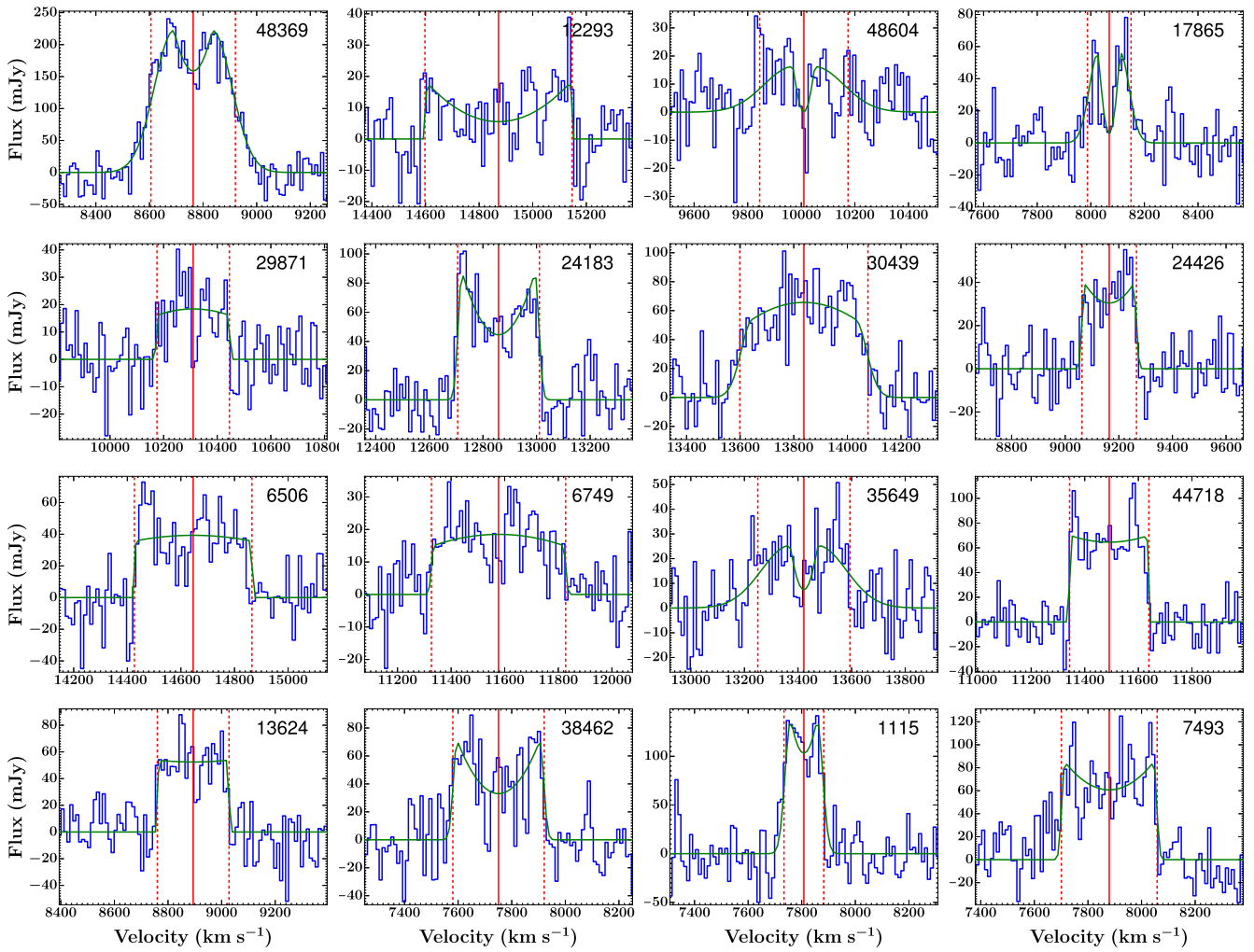


Figure C1 – continued

Downloaded from <http://mnras.oxfordjournals.org/> at University College London on August 19, 2016

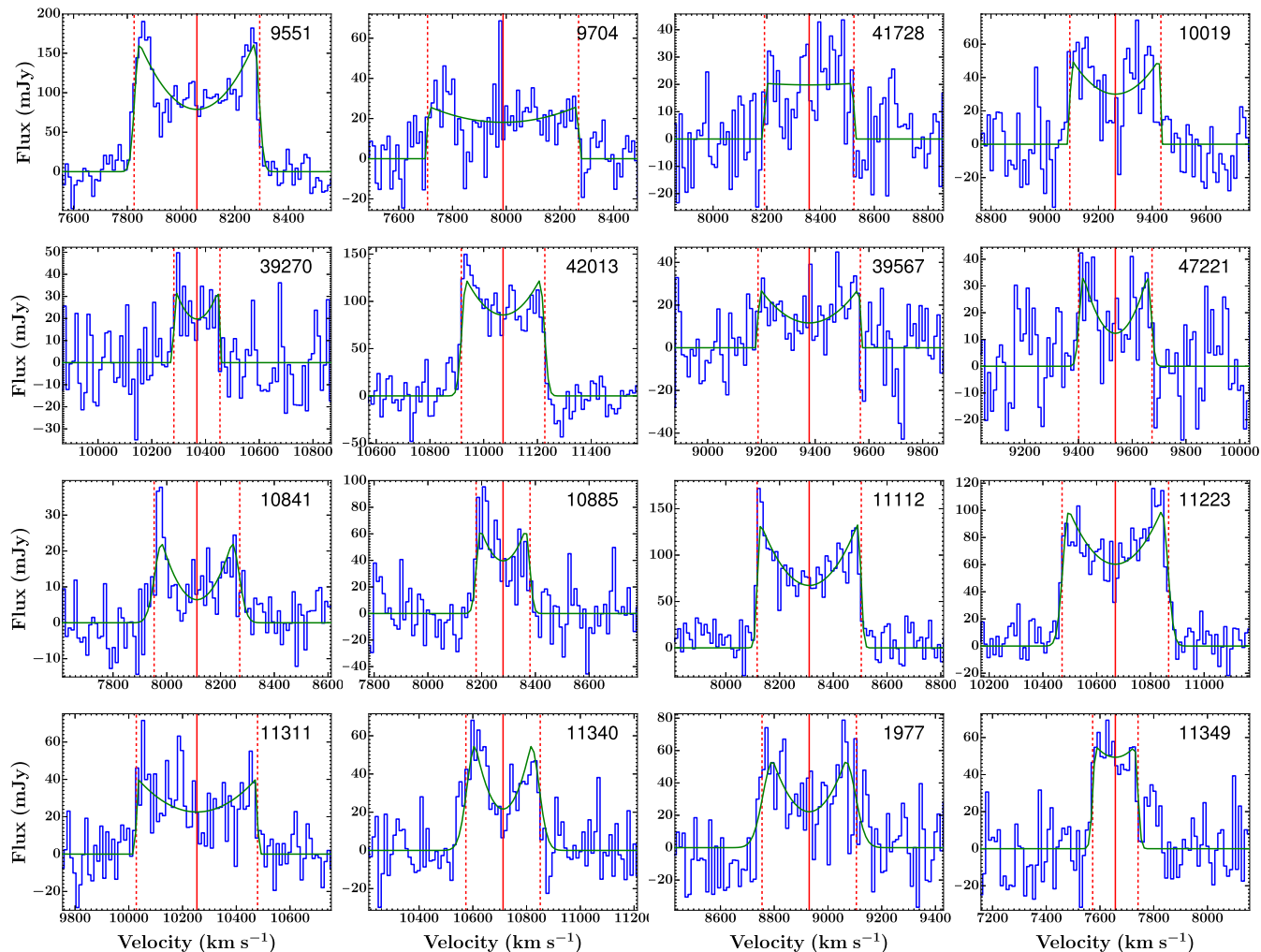


Figure C1 – *continued*

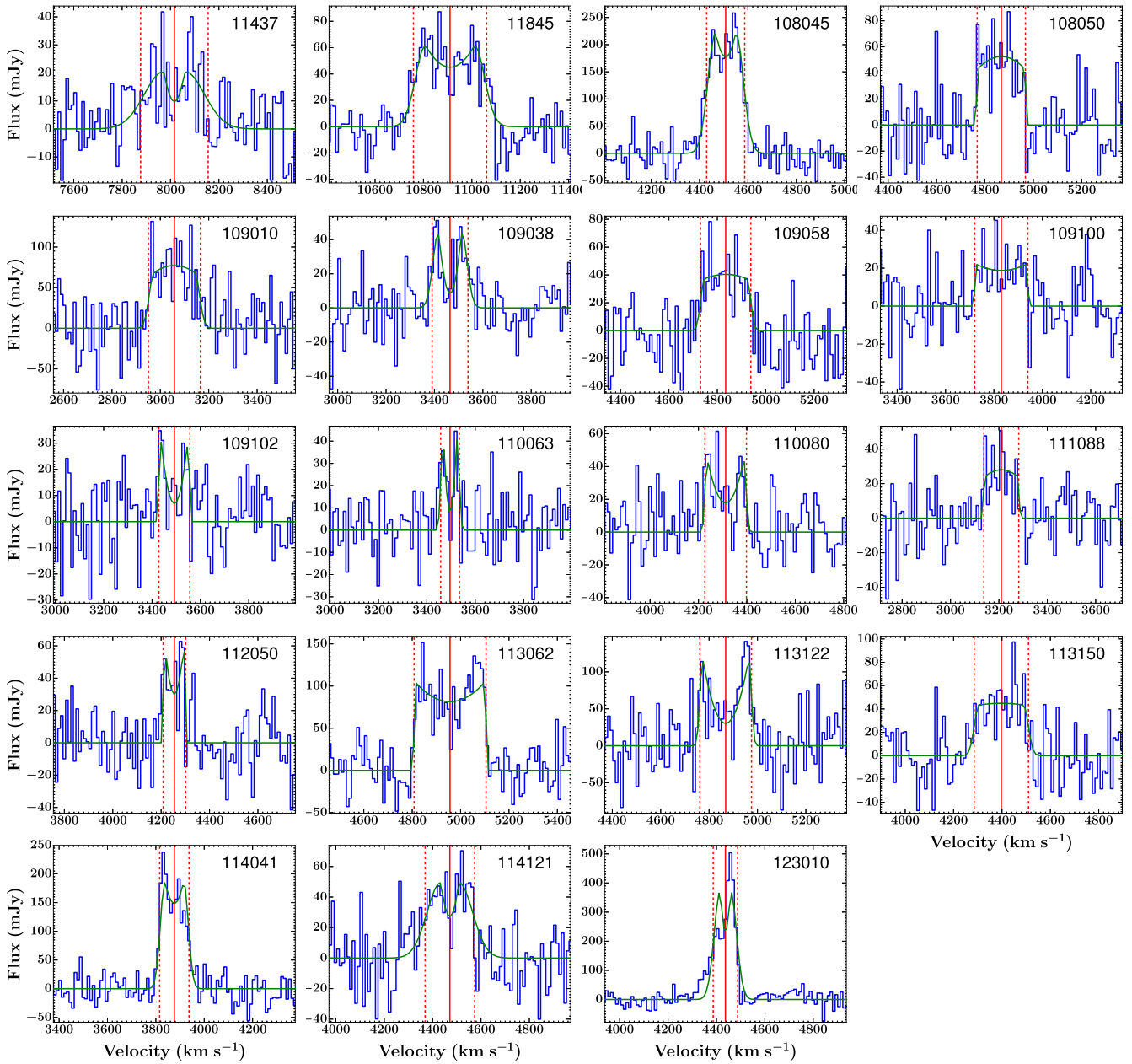


Figure C1 – continued

This paper has been typeset from a  $\text{\TeX}/\text{\LaTeX}$  file prepared by the author.

Downloaded from <http://mnras.oxfordjournals.org/> at University College London on August 19, 2016